



Numerical modeling of wave overtopping of damaged and upgraded rubble-mound breakwaters

M. Stagnitti ^{a,*}, J.L. Lara ^{b,*}, R.E. Musumeci ^a, E. Foti ^a

^a Department of Civil Engineering and Architecture, University of Catania, Catania, Italy

^b Instituto de Hidráulica Ambiental de Cantabria, Universidad de Cantabria, Santander, Spain

ARTICLE INFO

Keywords:

IH2VOF

Upgrading options

Wave overtopping discharge

Probability of wave overtopping

Overtopping volumes

ABSTRACT

Upgrade of aging harbor breakwaters is a worldwide problem, whose urgency is enhanced by the effects of climate change on coastal areas. In this context, the present work contributes to improve current understanding of the hydraulic response of damaged and upgraded rubble-mound breakwaters, providing also a methodology for the implementation of an ad-hoc prediction tool based on numerical simulations. The numerical model *IH2VOF*, which was calibrated using experimental data, proved to be a valid tool for the study of wave overtopping phenomena of structures with irregular armor slope or additional armor layers. The results confirmed that also for the non-conventional tested structures the wave sequence significantly affects the uncertainty of wave overtopping estimates when low-energy sea states are considered, more than the time series length. Site-specific formulas for the assessment of both mean wave overtopping discharge and probability were defined to overcome the limits of state-of-the-art formulations. Finally, traditional formulations for the description of the individual wave overtopping volumes based on the two-parameters Weibull distribution can be applied also to damaged and upgraded breakwaters.

1. Introduction

Maintenance and upgrade of existing harbor rubble-mound breakwaters is a hot-topic in coastal engineering, which deserve special attention because of the possible intensification of external loads due to the effects of climate change (Hughes, 2014; Toimil et al., 2020). Existing breakwaters, which may have experienced severe damages and several structural interventions during their lifetime, are usually non-conventional structures with complex geometries. Such structures generally present an irregular seaside slope and/or unusual layering due to the superposition of several mounds of different kinds of armor blocks. Common upgrading concepts, such as the addition of new armor units and/or the construction of emerged or submerged barriers at the toe of the existing structure (Burcharth et al., 2014), clearly further contribute to the non-conventional nature of existing breakwaters, in terms of both armor slope and structure porosity.

The irregularity of the armor slope typical of damaged breakwaters and the non-conventional porosity which characterizes both existing and upgraded breakwaters may significantly influence the wave–structure interaction, thus causing possible deviations of the breakwater behavior from the predictions of traditional formulations. The understanding of such processes can be achieved through specific

laboratory tests, which enable the analysis of the hydraulic response of the structure under controlled conditions (Burcharth et al., 2014; Foti et al., 2020). However, physical modeling usually needs proper testing facilities and funding. In particular, constructive problems in reproducing in the lab complex geometries at a proper scale may be particularly relevant. On the other hand, numerical modeling represents an efficient and flexible alternative for the simulation of the wave interaction with different kinds of coastal structures in a cost-effective manner.

In-depth understanding of wave overtopping of damaged and upgraded rubble-mound breakwaters is essential, since it directly influences the structure integrity and port operability (Koosheh et al., 2021). Despite the urgency of the problem, there is a lack of experimental and numerical investigations on the behavior of damaged or upgraded rubble-mound breakwaters. The possibility to apply state-of-the-art formulations to describe and predict wave overtopping of such non-conventional structures has not been verified yet, and new specific formulas should be defined. Indeed, only a few experimental campaigns on upgraded rubble-mound breakwaters exist, which did not aim to the definition of new specific empirical formulas for upgraded structures nor the validation of traditional ones (Reis et al., 2011; Santos-Ferreira

* Corresponding authors.

E-mail addresses: martina.stagnitti@unict.it (M. Stagnitti), lopezjav@unican.es (J.L. Lara), rosaria.musumeci@unict.it (R.E. Musumeci), enrico.foti@unict.it (E. Foti).

<https://doi.org/10.1016/j.oceaneng.2023.114798>

Received 9 March 2023; Received in revised form 22 April 2023; Accepted 7 May 2023

Available online 29 May 2023

0029-8018/© 2023 The Authors. Published by Elsevier Ltd. This is an open access article under the CC BY license (<http://creativecommons.org/licenses/by/4.0/>).

et al., 2015; Jensen et al., 2018), apart from the investigation presented by Stagnitti et al. (2020, 2023b).

In this context, the present work aims to assess whether state-of-the-art formulas for the description of wave overtopping phenomena of conventional structures can be successfully applied to damaged and upgraded rubble-mound breakwaters, also proposing improved empirical relationships if needed. In particular, the tested cube-armored breakwaters differ from conventional ones in terms of shape and thickness of the porous armor layer. Indeed, as opposite to the traditional rubble-mound structure armored with a single or double layer of cubes, the armor slope of the damaged cross-section considered here is irregular. Moreover, the studied upgraded structure with additional armor units and raised wave wall is characterized by more than two layers of cubes, i.e. by a porous armor layer thicker than conventional ones. For the first time, the *IH2VOF* model is calibrated and validated to study the response of a damaged existing structure and of its upgraded configuration. Results from the numerical model were used to build up a dataset of overtopping measurements. Regardless of the considered structure-type (i.e. vertical wall, smooth slope or rubble-mound breakwater), the analysis of wave overtopping must take into account the uncertainty induced by the length of the incident wave series and the phase distributions for the amplitude components of the wave spectrum (Pearson et al., 2002; McCabe et al., 2013; Williams et al., 2014; Romano et al., 2015; Williams et al., 2019). Therefore, for each tested condition, six different random seedings for the generation of iso-energetic sequences of waves were used, in order to preliminary quantify the uncertainty of mean wave overtopping discharge, probability of wave overtopping, and maximum overtopping volume as a function of the sea state energy content in the case of damaged or upgraded rubble-mound structures. Then the obtained wave overtopping data were compared with literature data and state-of-the-art formulas for the prediction of mean wave overtopping discharge and wave overtopping probability. In order to improve such formulas, the Iribarren number ($\xi_{m-1,0}$) was included together with new specific empirical coefficients.

The paper is organized as follows. In Section 2 a brief description of the employed numerical model is given. Section 3 presents the selected case study, i.e. the horizontally composite breakwater of the Port of Catania (Italy), and it provides an overview of the experimental data used for calibration and validation. The setup of the numerical domain, the calibration of the porosity parameters, the model validation and the performed simulations are described in Section 4. In Section 5, the effects of wave series sequence and length on wave overtopping of damaged and upgraded breakwaters are analyzed. The comparison between the obtained wave overtopping data and state-of-the-art formulas is discussed in Section 6. Finally, Section 7 draws the main conclusions of the work and gives suggestions for possible future developments.

2. Description of the numerical model

The hydraulic behavior of damaged and upgraded rubble-mound breakwaters was investigated by using the two-dimensional computational fluid dynamics (CFD) model *IH2VOF* (Lara et al., 2011a,b). Such a model has been successfully applied for the analysis of wave overtopping phenomena and wave induced load for traditional rubble-mound breakwaters (Losada et al., 2008), low crested rubble-mound breakwaters (Garcia et al., 2004; Losada et al., 2005; Lara et al., 2006), low-mound breakwaters (Lara et al., 2008; Guanche et al., 2009) and non-conventional breakwaters for wave energy conversion (Di Lauro et al., 2019, 2020). Recently, Lara et al. (2019) employed *IH2VOF* for the analysis of the evolution of the hydraulic performances of a historical non-conventional vertical breakwater with a low crested elevation.

IH2VOF solves the 2D RANS equations, based on the decomposition of the instantaneous velocity and pressure fields into their mean and

turbulent components (Lara et al., 2011a,b). Under this assumption, the RANS equations can be written as follows:

$$\frac{\partial \bar{u}_i}{\partial x_i} = 0 \quad (1)$$

$$\frac{\partial \bar{u}_i}{\partial t} + \bar{u}_j \frac{\partial \bar{u}_i}{\partial x_j} = -\frac{1}{\rho} \frac{\partial \bar{p}}{\partial x_i} + g_i + \frac{1}{\rho} \frac{\partial \bar{\tau}_{ij}}{\partial x_j} - \frac{\partial (\overline{u'_i u'_j})}{\partial x_j} \quad (2)$$

where $u_i = \bar{u}_i + u'_i$ and $p = \bar{p} + p'$ are respectively the Reynolds-decomposed velocity and pressure fields, ρ is the density of the fluid, g_i is the i th component of the gravitational acceleration and $\bar{\tau}_{ij}$ is the mean viscous stress tensor. The mean flow characteristics for turbulent conditions are calculated by solving the $k - \epsilon$ model, in which the coefficients proposed by Lin (1998) and Rodi (1993) are employed.

The flow inside the porous media is modeled by means of the VARANS equations, which are obtained by applying the intrinsic volume average to the RANS equations and combined with the Forchheimer's relationship (Liu et al., 1999):

$$\frac{\partial \langle \bar{u}_i \rangle}{\partial x_i} = 0 \quad (3)$$

$$\frac{\partial \langle \bar{u}_i \rangle}{\partial t} + \frac{\partial \langle \bar{u}_i \rangle \langle \bar{u}_j \rangle}{\partial x_j} = -\frac{1}{\rho} \frac{\partial \langle \bar{p} \rangle}{\partial x_i} + g_i + \frac{1}{\rho} \frac{\partial \langle \bar{\tau}_{ij} \rangle}{\partial x_j} - \frac{\partial \langle \overline{u'_i u'_j} \rangle}{\partial x_j} - \left[\frac{\alpha_F \nu (1-n)^2}{n^2 D_{n50}^2} \langle \bar{u}_i \rangle + \frac{\beta_F (1-n)}{n D_{n50}} \sqrt{\langle \bar{u}_1 \rangle^2 + \langle \bar{u}_2 \rangle^2} \langle \bar{u}_i \rangle + c_F \frac{1-n}{n} \frac{\partial \langle \bar{u}_i \rangle}{\partial t} \right] \quad (4)$$

where ν is the kinematic viscosity of the fluid, D_{n50} and n are respectively the median nominal diameter and the porosity of the porous media, α_F and β_F are two empirical coefficients associated with the linear and nonlinear porous drag force respectively, and c_F is the empirical parameter of the added mass coefficient, equal to 0.34. The coefficients α_F and β_F depend on several parameters, linked to both flow and structure characteristics. Since an accurate description of such dependencies is still not available for oscillatory flows, the best-fit values for α_F and β_F should be evaluated by comparing experimental data and numerical results (Losada et al., 2008).

The RANS, VARANS and $k - \epsilon$ equations are all solved using the finite differences two-steps projection method (Chorin, 1968, 1969). The computational domain is discretized in rectangular cells, whose dimensions can be uniform or different for each sub-region of the numerical channel. The movement of free surface is tracked by a VOF method. In addition, the insertion of solid boundaries of arbitrary shape in the computational domain can be performed through a partial cell treatment (Lara et al., 2011b).

Still water is the model initial condition for the mean flow in the whole domain, although specific form for the free surface displacement or mean velocity field can be introduced. As regards turbulence, non-zero initial values are generated using a chosen seed. At solid walls no slip or free slip boundary conditions can be used, whereas at the free surface the stress, pressure and gradients of turbulent energy (k) and dissipation (ϵ) are set equal to zero. Moreover, the open boundary condition can be employed to allow two-way flow, by defining free pressure and velocity. As regards the wave generation, three procedures are included in the model, i.e. internal wavemaker, static wave paddle (i.e. Dirichlet boundary condition) and dynamic wave paddle (i.e. moving boundary condition). Finally, wave absorption boundary conditions are available, which allow to run longer simulations, avoiding most of the effects of reflected waves inside the numerical flume. In particular, the active wave absorption can be applied to both the Dirichlet and the moving boundary conditions, whereas a sponge layer can be placed on the opposite side of the flume for passive absorption.



Fig. 1. Location and layout of the Port of Catania (Italy) and indication of the most representative cross-sections of the harbor breakwater (satellite view from Google Earth, 2022).

3. Overview of physical model experiments

The case study of the Catania harbor breakwater was selected to construct a dataset on the hydraulic behavior of non-conventional existing or upgraded rubble-mound breakwaters to be compared with the predictions of traditional formulations. The Port of Catania plays a fundamental role for the Italian economy, thanks to its barycentric position between the European and the North-African ports, the Suez Channel and the Strait of Gibraltar (see Fig. 1). The 2.25 km long outer breakwater represents the main protection for the harbor basin. Such a structure was constructed in the XVIII century as a composite breakwater (Franco, 1994; Oumeraci, 1994; Takahashi, 2002), and finally lengthened and rehabilitated as a rubble-mound structure using 62 t cubic armor units. Currently, the Catania harbor breakwater needs upgrading, since it is severely damaged and increasingly frequent excessive wave overtopping discharges occur, causing significant limitations to port activities.

Physical modeling of the existing Catania harbor breakwater and of five possible upgrading solution is described in details by Stagnitti et al. (2020, 2023b). Two-dimensional experiments were performed at the Hydraulic Laboratory of the University of Catania, using the 1:70 geometrical scale and considering two representative cross-sections, no. 10 and no. 40 in Fig. 1. The structure was placed on a flat sea bottom because of the very mild slope at the studied site. The tested upgrading solutions consist in the addition of extra armor units equal or smaller than the existing ones placed according to different patterns with a quarry stone toe berm, and/or in the rising of the wave wall crest level. A total of 192 two-dimensional tests were carried out inside a channel 18.00 m long, 1.20 m high and 2.40 m wide, built within a tank equipped with a flap-type wavemaker that enables the generation of random waves using JONSWAP spectra. For each tested configuration, five different sea states were simulated, which are summarized in Table 1 in terms of measured incident significant wave height (H_s), peak wave period (T_p), water depth (h) and number of waves (N_w), where sea state W4 represents the design wave conditions of the upgraded breakwater. Each sea state was divided into three equal intervals, characterized by a different seeding for the random wave generation, thus obtaining a total of 4500 waves. Experimental data regarding the wave characteristics were acquired through resistance gauges placed in front of the breakwater, and the reflection coefficient (k_r) was calculated using the four gauge method proposed by Faraci et al. (2015). Damage suffered by the outer armor layer was quantified using both traditional and novel techniques, based on the counting of the displaced blocks and

Table 1

Characteristics of the experimental incident wave motion.

| Sea state ID | H_s [m] | T_p [s] | h [m] | N_w [no. of waves] | No. of realizations |
|--------------|-----------|-----------|---------|----------------------|---------------------|
| W1 | 0.075 | 1.18 | 0.270 | 1500 | 3 |
| W2 | 0.071 | 1.24 | 0.270 | 1500 | 3 |
| W3 | 0.093 | 1.27 | 0.270 | 1500 | 3 |
| W4 | 0.100 | 1.27 | 0.270 | 1500 | 3 |
| W5 | 0.109 | 1.43 | 0.270 | 1500 | 3 |

on the novel analysis of the armor surface roughness, respectively. As suggested by Iuppa et al. (2019), a specially designed overtopping tank was placed behind the model for the continuous measurement of the water volumes which flow behind the structure crest, thus allowing the calculation of the mean overtopping discharge. Wave overtopping was measured considering 1500 waves, which is more than the minimum number of 500÷1000 waves suggested by EurOtop (2018).

In the present work, only a part of the experimental dataset presented by Stagnitti et al. (2020, 2023b) was employed for the calibration of the numerical model. In particular, the most offshore cross-section no. 40 is considered, which is the most exposed one to the wave motion (see Fig. 1). Two configurations were investigated: (i) the existing structure (see Fig. 2a); (ii) the upgrading option which offered the best hydraulic performances during the tests. The latter one involves the addition of extra armor blocks equal to the existing ones placed along a 2:1 slope with a quarry stone toe berm, and the rising of the wave wall by 0.015 m, which corresponds to 1.00 m at prototype scale (see Fig. 2b). Experimental results show that the higher wave wall and the wider crest of the upgraded structure strongly reduce the number of overtopped waves with respect to the existing breakwater, by 30% for the design wave condition. The thicker and regular armor layer also contributes to this reduction. Indeed, even if the calculated values of Iribarren number indicate the same collapsing wave breaking type of the existing structure, the addition of extra armor blocks removes any geometric irregularity, thus avoiding local steepening of the lowest waves and the consequent increase of wave overtopping. Moreover, the greater thickness of the armor layer intensifies wave dissipation thanks to the enhanced porosity. Finally, the presence of the toe berm supporting the additional armor units induces breaking of the highest waves. The experimental data on damage dynamics revealed that the breakwater slope did not change during the experimental tests. Therefore, the numerical simulations of the two configurations were considered with a fixed geometry.

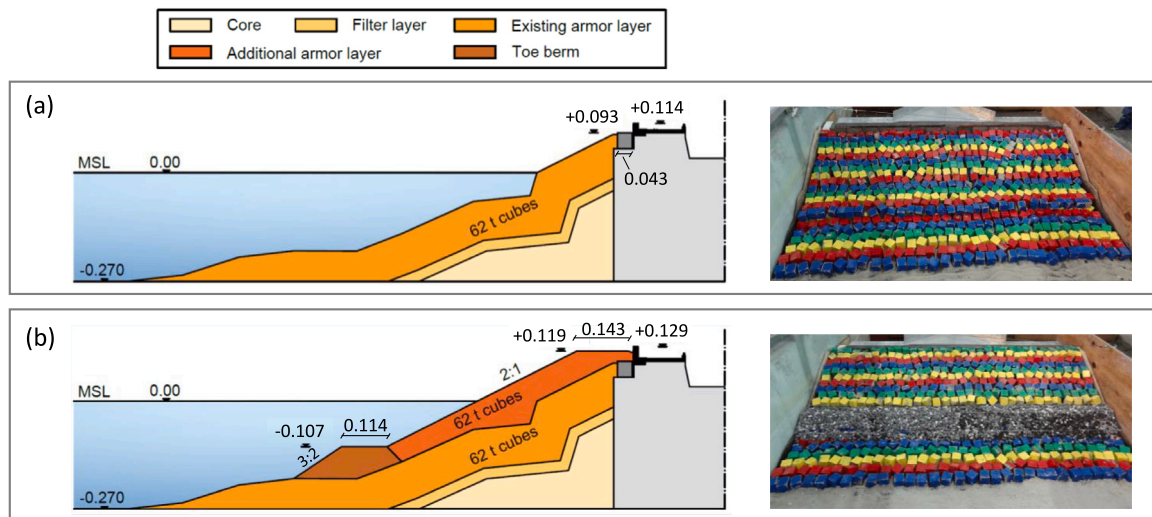


Fig. 2. Sketch and dry physical model of cross-section no. 40 of the Catania harbor breakwater: (a) existing structure; (b) upgraded structure with additional cubes equal to the existing ones and heightened wave wall.

4. Numerical model setup and simulations

In the present section, the characteristics of the employed numerical domain are described, in terms of geometry, computational grid and boundary conditions. Furthermore, the outputs of the calibration of the porosity parameters of the layers of both the existing and upgraded structures and the results of the model validation are discussed. Finally, the simulations performed to extend the numerical dataset on wave overtopping are presented.

4.1. Numerical domain

Two-dimensional simulations were carried out inside a numerical wave channel, whose height and length was fixed considering the dimension of the structure to be tested, which is about 1.60 m wide and 0.40 m high, and also the hydrodynamic conditions to simulate. Sea state W4 (see Table 1) was used as reference for the preliminary definition of the total length of the channel and of the numerical grid. In particular, the length of the numerical domain was set equal to the structure length plus one deep-water wavelength ($L = gT_p^2/2\pi$), i.e. 4.50 m, which was preliminary demonstrated to ensure the development of the wave motion with limited numerical dissipation and computational costs. The height of the domain was fixed equal to 0.65 m (i.e. the height of the structure plus 0.25 m), in order to avoid the influence of the top boundary on the wave overtopping phenomena. Fig. 3 shows a sketch of the numerical wave flume, the reference system, and the position of the free surface elevation and velocity gauges: (i) gauge no. 1 was placed one meter after the origin of the domain, in order to monitor the waves close to generation area; (ii) gauges no. 2, 3, 4 and 5 were located following the same arrangement of the lab tests for the evaluation of the reflection coefficient according to the four gauge method proposed by Faraci et al. (2015); (iii) gauge no. 6 was positioned at the toe of the structure; (iv) gauge no. 7 was placed in the correspondence of the wave wall, in order to measure the overtopping waves. The Dirichlet boundary condition was employed to generate irregular wave series using JONSWAP spectra. Moreover, active and passive wave absorption was applied to reduce wave reflection inside the flume.

A preliminary mesh sensitivity analysis was performed to select the proper Δx and Δy of the grid, considering the existing structure, a first rough estimate of its porosity (i.e. core: $D_{n50} = 0.009$ m, $n = 0.32$, $\alpha_F = 200$, $\beta_F = 1.20$, $c_F = 0.34$; filter: $D_{n50} = 0.017$ m, $n = 0.35$, $\alpha_F = 200$, $\beta_F = 2.00$, $c_F = 0.34$; existing armor layer: $D_{n50} = 0.059$ m, $n = 0.47$,

$\alpha_F = 200$, $\beta_F = 0.60$, $c_F = 0.34$), and sea states W1 and W4 (see Table 1). Two uniform grids were tested, having $\Delta x = 0.020$ m and $\Delta y = 0.010$ m and $\Delta x = 0.010$ m and $\Delta y = 0.005$ m, respectively. Both grids ensure the aspect ratio (i.e. $\Delta x/\Delta y$) equal to 2, as well as at least 10 and 20 cells per wave height along the vertical direction, respectively. The incident wave spectra obtained from simulations performed with the finer and coarser grids were almost identical. Nevertheless, the simulation of wave overtopping is affected by the grid cell size. Indeed, the non-dimensional mean wave overtopping discharge ($q^* = q/\sqrt{gH_s^3}$) of the coarser grid simulations is about 15% of q^* of the finer grid simulations. However, both the calculation grids provide q^* comparable with the experimental and predicted values, thus demonstrating their adequacy in reproducing wave overtopping of the tested structures. Since the calculation times of the coarser grid are one order of magnitude smaller than the ones of the finer grid, the former was chosen for the final setup of the numerical model. The domain contains a total of 226 and 66 cells along the x and y directions, respectively. The time step is dynamically adjusted during the simulations depending on the Courant number, Δt ranging between 0.02 s to 0.06 s. The numerical output data of the wave and velocity gauges is re-sampled at 30 Hz by linear interpolation. Using a processor Intel Xeon Silver 4214 2.20 GHz, about 250 waves were reproduced every thirty minutes.

4.2. Calibration of the porosity parameters

About 80 simulations were run to calibrate the porosity parameters of Eq. (4) for each layer of the rubble-mound structure, using as benchmark the results of the experimental campaign briefly described in Section 3. The five experimental wave conditions summarized in Table 1 were reproduced. The porosity of the structure was preliminary demonstrated not to influence the shape of the incident wave spectra. Therefore, the comparison between experimental and numerical incident wave motion calculated through the four gauge method (Faraci et al., 2015) applied to gauges no. 2, 3, 4 and 5 was performed for the tests with existing structure, considering the first rough estimate of its porosity presented in Section 4.1. Fig. 4 shows the percentage difference between numerical and experimental incident significant wave height (H_s), peak wave period (T_p) and spectral wave period ($T_{m-1,0}$), which was demonstrated to significantly influence the wave overtopping phenomena (van Gent, 1999). The numerical values of H_s underestimate the experimental ones, with absolute value of the percentage differences in the range 2.5÷13.0% (see Fig. 4a). As regards T_p , the percentage error between numerical and experimental values is

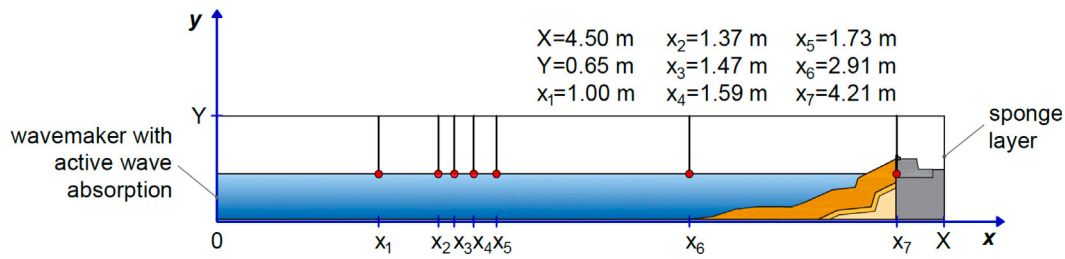


Fig. 3. Sketch of the numerical domain and location of the free surface and velocity gauges.

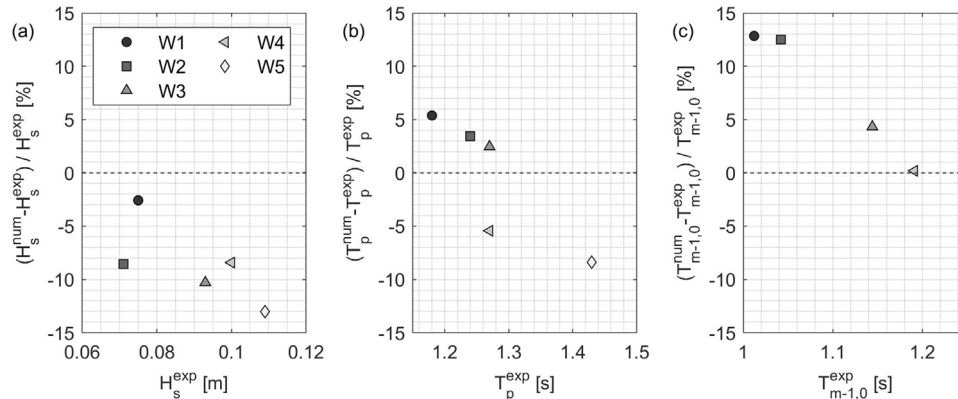


Fig. 4. Percentage error between numerical and experimental incident (a) significant wave height (H_s), (b) peak wave period (T_p) and (c) spectral wave period ($T_{m-1,0}$), which were calculated through the four gauge method (Faraci et al., 2015) applied to gauges no. 2, 3, 4 and 5.

Table 2
Wave energy of the experimental and numerical incident wave spectra.

| Incident wave energy [m ²] | W1 | W2 | W3 | W4 | W5 |
|--|-----------------------|-----------------------|-----------------------|-----------------------|-----------------------|
| Experimental | 7.94×10^{-5} | 8.88×10^{-5} | 1.37×10^{-4} | 1.57×10^{-4} | 1.89×10^{-4} |
| Numerical | 6.63×10^{-5} | 8.45×10^{-5} | 1.10×10^{-4} | 1.30×10^{-4} | 1.40×10^{-4} |

smaller, being its absolute values not higher than 8.4% (see Fig. 4b). Finally, the numerical $T_{m-1,0}$ tends to overestimate the experimental one, with a percentage error not higher than 13.0% (see Fig. 4c). The differences between numerical and experimental H_s , T_p and $T_{m-1,0}$ are due to not only numerical dissipation which develops along the channel, but also discrepancies between the incident wave spectra. For instance, Fig. 5 compares the experimental incident wave spectra measured for sea states W1 and W4 (see Table 1). The numerical model is not able to capture the energy of the experimental spectra which corresponds to frequencies higher than 1 Hz. Three main factors can influence the performance of the numerical model in reproducing the experimental waves: (i) differences between the laboratory signal and the numerical one, and also between wave generation procedures; (ii) the model does not simulate the interactions between waves and the structure armor units, which would generate reflected high frequency small waves; (iii) laboratory tests were carried out without active wave absorption, contrary to numerical simulations. Nevertheless, the highest waves, which represent the main contribution to overtopping volumes, correspond to frequencies lower than 1 Hz. Moreover, the energy content of corresponding laboratory and numerical spectra are almost the same, as showed in Table 2. Therefore, the latter have been used for the calibration of the porosity parameters based on the experimental reflection coefficients and mean wave overtopping discharge.

Parameters α_F and c_F of Eq. (4) were fixed and respectively equal to 200 and 0.34, according to Lara et al. (2008). Concerning the porosity n , preliminary analyses revealed that the use of the experimental values for the existing and additional armor layers caused significant discrepancies between experimental and numerical mean

wave overtopping discharge. This is likely due to the fact that the outer armor blocks of the physical model were placed according to an almost regular pattern (see Fig. 2), which is similar to the one of the real structure, thus enhancing wave reflection and overtopping. The deviation of the numerical mean wave overtopping discharges from the experimental ones may be also due to limits in modeling the run-up and breaking processes over the structure. Therefore, we decided to induce porosity values of the existing and additional armor layer lower than the experimental ones. Eight different reasonable combinations of parameters n and β_F were tested for the existing structure, and other eight for the additional armor layer with toe berm, based on state-of-the-art suggestions. In particular, β_F generally ranges between 0.80 and 3.00 for rubble-mound breakwaters under wave attack, but values up to 11.0 can characterize variety of rock materials (Losada et al., 2016). The porosity n generally varies over a wide range for the core and the filter layer, whereas it is usually close to 0.47 for cubic or Antifer armor units (Massie, 1976). Values of n of the armor layer equal or lower than 0.30 indicate a very regular and paved placements of the blocks, as in the present case (Vieira et al., 2021). Thus, here the ranges of tested n are 0.32÷0.40 for core, filter layer and toe berm, 0.30÷0.47 for the existing armor layer and 0.25÷0.30 for the additional one. Instead, the tested values of β_F are 1.20 for the core, 2.00 for the filter layer, 1.20÷3.00 for the toe berm, 0.60÷3.00 for the existing armor layer and 1.20÷5.00 for the additional one. The employed procedure for the calibration of the porosity parameters was made up of two steps. First, the combinations of n and β_F which provide the greatest accordance between numerical and experimental reflection coefficients were identified. Then, the combination of n and β_F which ensured the best

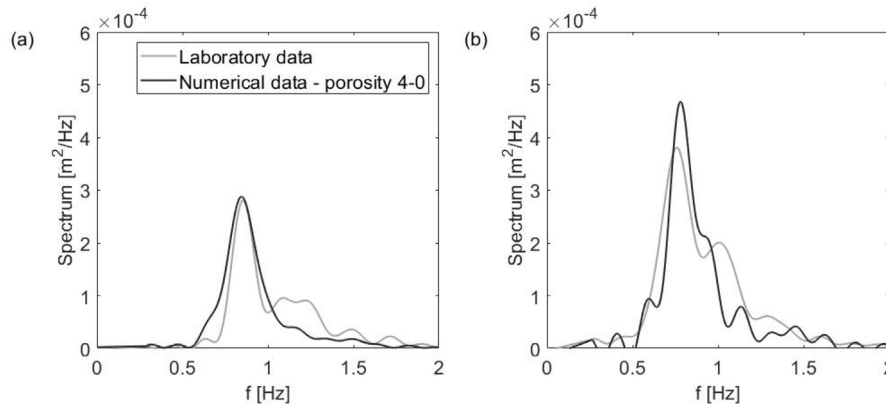


Fig. 5. Comparison between the experimental and numerical incident wave spectra: (a) sea state W1; (b) sea state W4.

Table 3
Characteristics of the porous layers of the tested structures.

| Layer | D_{n50} [m] | n [-] | α_F [-] | β_F [-] | c_F [-] |
|------------------------|------------------|------------|-------------------|------------------|--------------|
| Core | 0.009 | 0.32 | 200 | 1.20 | 0.34 |
| Filter | 0.017 | 0.35 | 200 | 2.00 | 0.34 |
| Existing armor layer | 0.059 | 0.30 | 200 | 1.50 | 0.34 |
| Additional armor layer | 0.059 | 0.25 | 200 | 5.00 | 0.34 |
| Toe berm | 0.017 | 0.35 | 200 | 3.00 | 0.34 |

correspondence between experimental and numerical mean wave overtopping discharge was selected among them. Reflection coefficients and mean overtopping discharges were evaluated for simulations with 1500 generated waves, similarly to the experimental tests. Such a procedure was first applied for existing core, filter and armor layer, and then for additional armor layer and toe berm. The selected combinations of n and β_F produced significant variations of the resulting non-dimensional mean wave overtopping discharge q^* . Indeed, the obtained values of q^* differ from each other by up to 3 times. Moreover, for the less energetic sea states (i.e. $R_c/H_s \geq 1.50$, being R_c the maximum value between the crest level and the crown wall height referred to MSL), q^* assumes null or non-null values ($O(10^{-6} \pm 10^{-5})$) depending on the considered combination of porosity parameters. Table 3 reports the chosen porosity parameters. The porosity n was set equal to 0.30 and 0.25 for the existing and additional armor layer, respectively, with D_{n50} of the cubic armor blocks equal to the size of the units employed for the construction of the physical model.

4.3. Sensitivity of numerical model predictions to individual wave characteristics

The adequacy of the chosen porosity parameters was further verified through the simulation of other five realizations of each simulated sea state, using different seedings for the random generation of the wave series to take into account the influence of the individual wave characteristics. In particular, the parameter H_{max}/H_s is representative of the randomness of each wave sequence, being H_{max} the maximum wave height. In the present work, H_{max}/H_s varies between 1.66 and 2.00.

Figs. 6a and c show the comparison between the numerical and experimental reflection coefficients (k_r) measured for the existing and upgraded structures, respectively, with reference to the different seeding realizations. The vertical and horizontal error bars indicate the corresponding standard deviation. For both tested configurations, the numerical data agree fairly well with the experimental ones. On average, the numerical model produced a slight overestimation of k_r , as demonstrated by the low normalized bias (NBI), which is likely due to the imperfect correspondence between experimental and numerical sea

states. Figs. 6b and d show the comparison between the experimental and numerical k_r expressed as a function of the Iribarren parameter $\xi_{m-1,0} = \tan \alpha / \sqrt{s_{m-1,0}}$, where α is the angle of the mean armor layer slope with respect to the horizontal plane and $s_{m-1,0} = 2\pi H_s / g T_{m-1,0}^2$. The angle of the mean armor slope α is given by the cotangent of the ratio between the horizontal distance from the start and end points of the slope and the difference in elevation of the same points. For the damaged cross-section, α is measured between the most offshore point of the crest of the structure and the point where the armor units start to be placed horizontally. Instead, for the upgraded cross-section, α is measured between the most offshore point of the crest and the contact point between armor layer and toe berm. In both cases, α is equal to about 30°. The empirical prediction formula proposed by Zanuttigh and van der Meer (2008) is also plotted as reference, considering a roughness factor γ_f of the cubic armor layer equal to 0.47 (EurOtop, 2018). The numerical values of $\xi_{m-1,0}$ are higher than the experimental ones mainly as a consequence of the tendency of the numerical model to overestimate the experimental $T_{m-1,0}$ (see Fig. 4c), and to a lower extent due to the absence of wave absorption in the physical lab. Despite this difference between numerical and experimental sea states, the numerical k_r clearly follow the same pattern of the experimental data for both existing and upgraded structures, thus confirming the choice of the porous media flow parameters. The Zanuttigh and van der Meer (2008) method slightly overestimates k_r of the existing structure and, to a lower extent, of the upgraded one (with NBI equal to 0.15 and 0.06 for the experimental and numerical data, respectively), probably due to the fact that such equations were calibrated considering data valid for newly built breakwaters. Here, the irregular shape of the damaged rubble-mound structure causes lower reflection than a regular slope. As regards the configuration with the upgraded armor layer, the differences between predicted and experimental reflection coefficients can be due to the influence of the complex layering, which increases the overall porosity of the structure.

Figs. 7a and c show the comparison between the numerical and experimental non-dimensional mean wave overtopping discharge q^* acquired for the existing and upgraded structures, respectively. Following the same approach employed to plot the k_r data, q^* corresponding to each simulated sea state is represented in terms of its numerical and experimental mean and standard deviation calculated using the acquired data for the different seeding realizations. Numerical q^* is quite similar to the experimental one. A commonly employed methodology to quantify the correspondence between measured and simulated non-dimensional mean wave overtopping discharge consists in calculating error indexes using the logarithm of q^* (Molines and Medina, 2016; Etemad-Shahidi et al., 2022; Mata and van Gent, 2023). The NBI is equal to 0.04 and -0.05 for the existing and upgraded structures, respectively. Also in this case, the lack of perfect correspondence between numerical and experimental measurements is likely due to

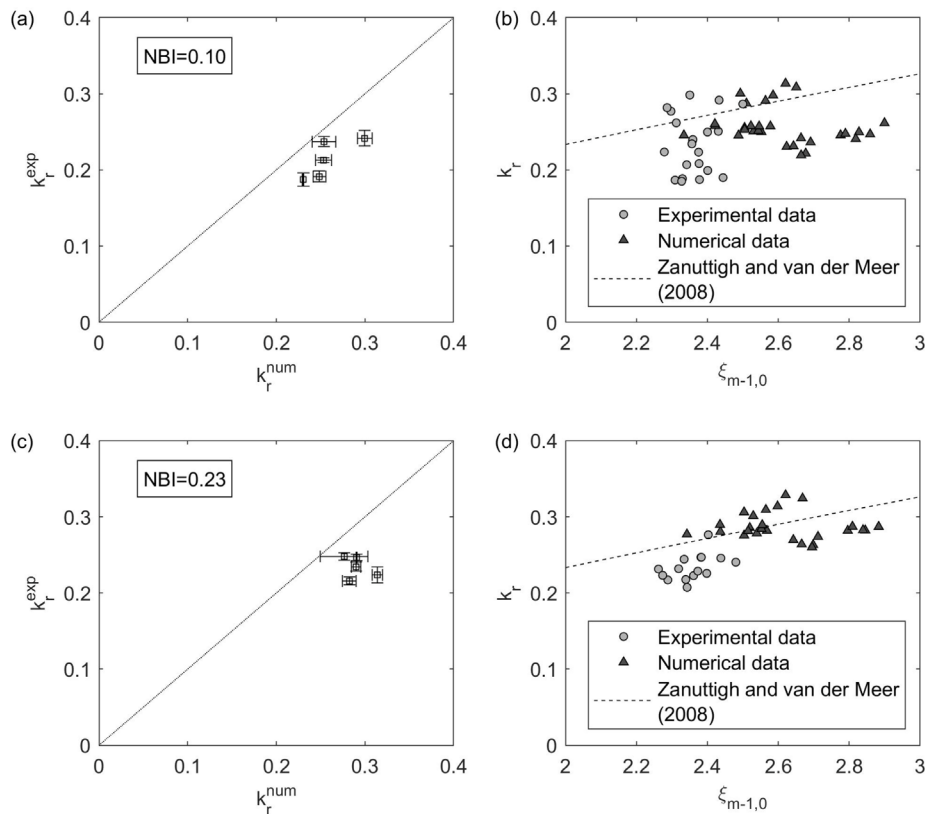


Fig. 6. Comparison between numerical and experimental reflection coefficients: experimental k_r vs numerical k_r measured for the (a) existing and (c) upgraded structure; experimental and numerical k_r measured for the (b) existing and (d) upgraded structure expressed as a function of the Iribarren number ($\xi_{m-1,0}$), with the equation suggested by Zanuttigh and van der Meer (2008) used as reference.

the tendency of the numerical model to overestimate the experimental $T_{m-1,0}$ (see Fig. 4c). Figs. 7b and d compare the experimental and numerical q^* expressed as a function of the non-dimensional structure freeboard (R_c/H_s), for the two tested configurations of the breakwater. The following state-of-the-art formula proposed by EurOtop (2018) is also plotted as reference:

$$q^* = \frac{q}{\sqrt{gH_s^3}} = a_E \cdot \exp \left[- \left(b_E \cdot \frac{R_c}{H_s \gamma_f} \right)^{1.3} \right] \quad (5)$$

where q is the mean wave overtopping discharge per meter, g is the gravitational acceleration, a_E and b_E are empirical parameters, respectively equal to 0.09 with standard deviation (σ) equal to 0.0135 and 1.50 with σ equal to 0.1500, and γ_f is the roughness factor equal to 0.47 for double layer of artificial cubes. The numerical model seems to reproduce quite well the behavior of the laboratory structures. Eq. (5) seems to better agree with the experimental and numerical data for q^* in the range $10^{-5} \div 10^{-3}$. Instead, the EurOtop (2018) formula produces an underestimation of both the experimental and numerical q^* of the upgraded structure. It should be noted that the discrepancies between the lower numerical q^* and the predictions of Eq. (5) are observed for values under the zero-overtopping limit defined by EurOtop (2018) for experimental tests, i.e. $q^* = 10^{-5}$. Such a limit was set after noticing that, considering the large experimental dataset employed to calibrate Eq. (5), q^* rarely exceeded it. Since Eq. (5) is not able to capture q^* lower than 10^{-5} , the disagreement between numerical and predicted values appears reasonable. Instead, the discrepancies between observed q^* higher than 10^{-3} and the predictions of the state-of-the-art formulas may be due to the non-conventional shape and porosity of the tested cross-sections, as further discussed in Section 6.

4.4. Extended numerical database

The calibrated numerical model was employed to further extend the wave overtopping database, in order to perform an in-depth investigation on the hydraulic response of damaged and upgraded structures. Table 4 reports the reference sea states used for the definition of the input hydrodynamic conditions, in terms of significant wave height, peak wave period, water depth and number of waves, which corresponds to $\xi_{m-1,0}$ ranging between 2.16 and 3.15. Besides sea states NW1–5, which coincide with the experimental sea states W1–5 reported in Table 1, other three reference sea states were defined to expand the range of hydrodynamic conditions, considering H_s equal to 95%, 105% and 120% of the design one (i.e. of H_s of sea state NW4) and T_p equal to 1.30 s. More energetic sea states could be tested, but they would be non-realistic for the studied site, even in the presence of climate change. Indeed, the significant wave height is expected to decrease in the future at the site of Catania (Stagnitti et al., 2022, 2023a). Sea states with H_s lower than 0.071 m (i.e. H_s of sea state NW2) were not simulated, because preliminary analysis revealed that in such cases wave overtopping is null for both the existing and upgraded breakwaters. Table 5 summarizes the performed simulations, in terms of input sea state, tested structure and number of realizations with different seedings for the random wave generation. All the sea states reported in Table 4 were reproduced, also considering variations of the water depth and of the peak wave period equal to ± 0.020 m and ± 0.20 s, respectively. For each input sea state, six realizations have been generated, in order to analyze the effects on overtopping phenomena due to: (i) wave-wave interaction; (ii) influence of wave sequence; (iii) the ratio between the maximum and the significant wave height of the series (H_{max}/H_s). The latter may be relevant for low overtopping events.

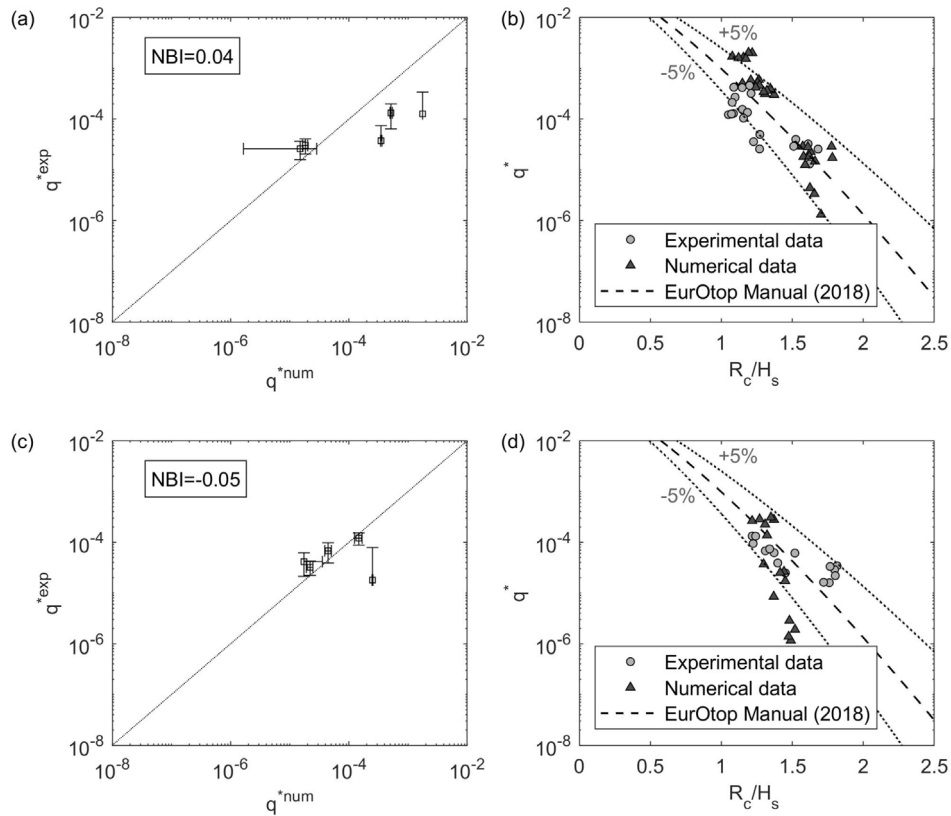


Fig. 7. Comparison between numerical and experimental non-dimensional mean wave overtopping discharge: experimental q^* vs numerical q^* measured for the (a) existing and (c) upgraded structure; experimental and numerical q^* measured for the (b) existing and (d) upgraded structure expressed as a function of the structure dimensionless freeboard (R_c/H_s), with the equation suggested by EurOtop (2018) and its 95% confidence bounds used as reference.

Table 4
Reference sea states used for the definition of the input hydrodynamics of the numerical simulations.

| Sea state ID | H_s [m] | T_p [s] | h [m] | N_W [no. of waves] |
|--------------|-----------|-----------|---------|----------------------|
| NW1 | 0.075 | 1.18 | 0.270 | 1500 |
| NW2 | 0.071 | 1.24 | 0.270 | 1500 |
| NW3 | 0.093 | 1.27 | 0.270 | 1500 |
| NW4 | 0.100 | 1.27 | 0.270 | 1500 |
| NW5 | 0.109 | 1.43 | 0.270 | 1500 |
| NW6 | 0.095 | 1.30 | 0.270 | 1500 |
| NW7 | 0.105 | 1.30 | 0.270 | 1500 |
| NW8 | 0.120 | 1.30 | 0.270 | 1500 |

Table 5
Summary of the input hydrodynamics of the performed simulations.

| Sea state | Tested structure | No. of realizations |
|-------------------------|------------------|---------------------|
| NW1-5 | existing | 6 |
| NW1-5 with $h+0.020$ m | existing | 6 |
| NW1-5 with $h-0.020$ m | existing | 6 |
| NW1-5 with $T_p+0.20$ s | existing | 6 |
| NW1-5 with $T_p-0.20$ s | existing | 6 |
| NW4-8 | upgraded | 6 |
| NW4-8 with $h+0.020$ m | upgraded | 6 |
| NW4-8 with $h-0.020$ m | upgraded | 6 |
| NW4-8 with $T_p+0.20$ s | upgraded | 6 |
| NW4-8 with $T_p-0.20$ s | upgraded | 6 |

A total of 300 simulations were performed, which allowed the analysis of the wave overtopping phenomena for both the existing and upgraded structures. Besides the mean wave overtopping discharge, which was measured also during the experimental campaign,

the probability of wave overtopping was evaluated. Moreover, parameters describing the individual wave overtopping volumes distribution were calculated for each simulated sea state.

5. Effects of the wave sequence and length on wave overtopping phenomena

The analysis of the influence of the wave sequence and length on wave overtopping phenomena is fundamental. First, the effects of the wave sequence on non-dimensional mean wave overtopping discharge, probability of wave overtopping and maximum overtopping volume of the damaged and upgraded structures were investigated, considering simulations 1500 waves long. Then, the variation of such measured quantities and of uncertainty for increasing number of generated waves were analyzed.

5.1. Effects of the wave sequence

The assessment of the influence of the characteristics of individual waves of randomly generated series on overtopping phenomena is useful to estimate the uncertainty which affects the results obtained through numerical modeling. As already stated in Section 4.2, the parameter H_{max}/H_s is representative of the differences between wave sequences having the same energy spectra. In the present study, H_{max}/H_s ranges between 1.66 and 2.00. The extent of variability of overtopping parameters corresponding to different realizations of the same sea state is quantified here through the coefficient of variation (CV), which is defined as the ratio between the standard deviation and the mean of the considered sample. A high CV indicates a great dispersion of the data.

In order to identify possible dependencies of CV of wave overtopping descriptors on the sea state energy content, its variation with

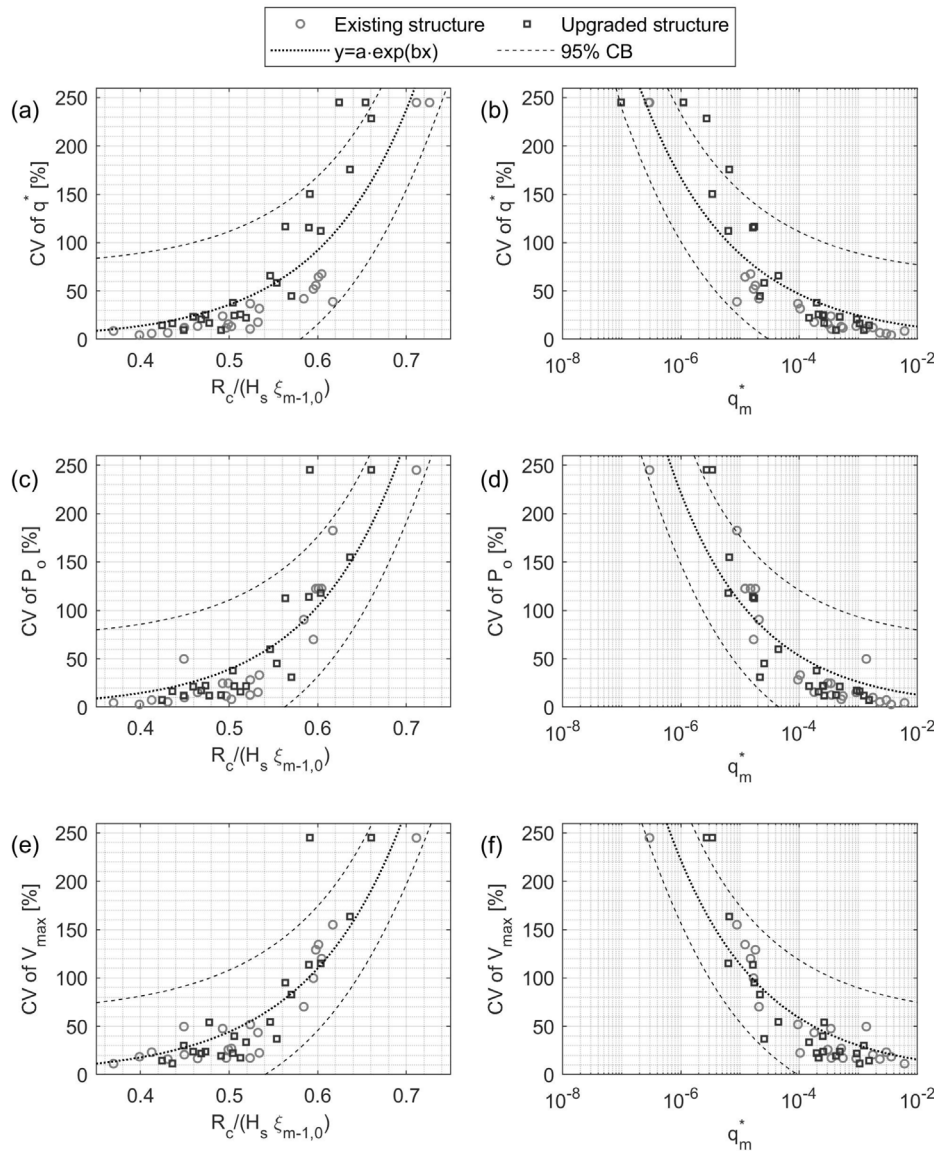


Fig. 8. Coefficient of variation of the measured numerical q^* , P_o and V_{max} expressed as a function of (a, c, e) the dimensionless structure freeboard $R_c/(H_s \xi_{m-1,0})$ and (b, d, f) of q_m^* . The dotted lines represent the fitted law, whereas the dashed lines are the corresponding 95% confidence bounds.

respect to the incident wave characteristics was analyzed. Figs. 8a,c and e show CV of the non-dimensional mean wave overtopping discharge (q^*), of the probability of wave overtopping ($P_o = N_o/N_w$, where N_o is the number of overtopping waves) and of the maximum wave overtopping volume (V_{max}), respectively, as a function of the non-dimensional structure freeboard $R_c/(H_s \xi_{m-1,0})$ for both the existing and upgraded structures. The introduction of the Iribarren number allows a better description of the wave overtopping processes, including the effects due to the breaking of waves over the structure slope and the dependence on wave period especially relevant in the maximum wave overtopping volume, which may be particularly significant for small overtopping events. Despite the limited range of $\xi_{m-1,0}$ investigated here, the inclusion of such a parameter in the assessment of the dependency of CV of wave overtopping measurements on the sea state energy content allows possible applications of the proposed approach to a wider range of wave conditions. The results reveal that CV of the three considered overtopping descriptors increases with $R_c/(H_s \xi_{m-1,0})$, according to an exponential law. Table 6 shows the estimate and the 95% confidence upper and lower bounds (CB_{up} and CB_{low} , respectively) of the coefficients of the models fitted through the least squares method, and the corresponding coefficient of determination (R^2). The

observed increasing trend of CV with $R_c/(H_s \xi_{m-1,0})$, which is almost the same for the three studied overtopping descriptors, indicates that the uncertainty in the estimate of q^* , P_o and V_{max} is higher for less energetic incident waves, for which the influence of H_{max}/H_s is more significant. In particular, it was found that: (i) for $R_c/(H_s \xi_{m-1,0})$ not greater than 0.50, CV is smaller than 50%; (ii) when $R_c/(H_s \xi_{m-1,0})$ ranges between 0.50 and 0.60, CV has values between 50% and 150%; (iii) for $R_c/(H_s \xi_{m-1,0})$ greater than 0.60, values of CV up to 250% are reached.

In order to allow the immediate estimation of CV corresponding to fixed values of non-dimensional mean wave overtopping discharge, its variation with respect to the mean q^* calculated for the six realizations of each simulated sea state (q_m^*) was also investigated. Figs. 8b, d and f show that CV of q^* , P_o and V_{max} decreases with increasing q_m^* according to three similar exponential laws, whose coefficients and R^2 calculated through the least squares method are reported in Table 6. Such a result is in accordance with the findings concerning the variation of CV with increasing $R_c/(H_s \xi_{m-1,0})$. Indeed, q^* and $R_c/(H_s \xi_{m-1,0})$ are inversely correlated, since to less energetic sea states correspond lower overtopping discharges. Also in this case, three regions can be identified in the plots of Fig. 8b, d and f: (i) for q_m^* not greater than 5×10^{-6} ,

Table 6

Coefficients and coefficient of determination of the fitted laws which describe how CV of q^* , P_o and V_{max} varies with $R_c/(H_s \xi_{m-1,0})$ and q_m^* .

| Law | A | | | B | | | R^2 |
|---|----------|---------------|----------------|----------|---------------|----------------|-------|
| | Estimate | 95% CB_{up} | 95% CB_{low} | Estimate | 95% CB_{up} | 95% CB_{low} | |
| $R_c/(H_s \xi_{m-1,0})$ - CV of q^* | 0.312 | -0.054 | 7.698 | 9.478 | 0.679 | 11.256 | 0.75 |
| $R_c/(H_s \xi_{m-1,0})$ - CV of P_o | 0.287 | -0.053 | 7.956 | 9.818 | 0.628 | 11.679 | 0.75 |
| $R_c/(H_s \xi_{m-1,0})$ - CV of V_{max} | 0.464 | 0.008 | 7.552 | 9.115 | 0.919 | 10.679 | 0.78 |
| q_m^* - CV of q^* | 3.637 | 1.478 | -0.736 | -0.638 | 5.797 | -0.540 | 0.82 |
| q_m^* - CV of P_o | 3.068 | 0.987 | -0.837 | -0.713 | 5.150 | -0.589 | 0.78 |
| q_m^* - CV of V_{max} | 4.116 | 1.813 | -0.768 | -0.665 | 6.421 | -0.561 | 0.80 |

values of CV up to 250% are reached; (ii) when q_m^* ranges between 5×10^{-6} and 1×10^{-4} , CV assumes values between 50% and 150%; (iii) for q_m^* greater than 1×10^{-4} , CV is not greater than 50%.

In conclusion, the uncertainty in the estimation of the wave overtopping phenomena increases with decreasing energy content of the incident wave motion also for damaged and upgraded structures, in accordance with the findings of Pearson et al. (2002), Romano et al. (2015) and Williams et al. (2014, 2019) for conventional breakwaters, and following an exponential law. Such an uncertainty affects both averaged (i.e. q^*) and not-averaged (i.e. P_o and V_{max}) overtopping descriptors. In order to ensure a CV of the overtopping measurements smaller than 50%, $R_c/(H_s \xi_{m-1,0})$ lower than 0.50 or q^* greater than 10^{-4} should be considered.

5.2. Effects of the number of waves

The analysis of the influence of the length of the time series on wave overtopping descriptors was performed considering the mean values of q and P_o evaluated for the six realizations of each simulated sea state, namely q_m and $P_{o,m}$. The maximum overtopping volume was not studied, since it depends on the wave sequence rather than on the time-averaged energy content of the incident wave motion. In order to carry out such an analysis, a number of shorter time series were extracted from the simulated ones, considering 18 windows having progressively increasing width, with states of about 80 waves. For each sub-series, the mean wave overtopping discharge and the probability of wave overtopping was calculated. Then, the mean values q_m , $P_{o,m}$ and the corresponding CV were evaluated for each simulated sea state.

Figs. 9a–b show the variation of CV of q and P_o as a function of N_w , considering four representative wave conditions. The coefficient of variation of q exhibits a clear decreasing trend for increasing N_w (see Fig. 9a). Indeed, for the same $R_c/(H_s \xi_{m-1,0})$ the effects of the individual wave characteristics are less clear when longer wave series are considered. For each tested wave condition, CV of q tends to be stable only after 750 waves. Moreover, as discussed in Section 5.1, q measured for the highest $R_c/(H_s \xi_{m-1,0})$ (i.e. less energetic sea states) is characterized by a significantly greater CV . It should be noted that the length of the time series contributes to the reduction of CV to a greater extent for small $R_c/(H_s \xi_{m-1,0})$. Such a result is due to the fact that for the less energetic sea states the influence of the wave sequence is far more significant than the effects of the number of waves. The above-discussed findings are valid also for CV of P_o (see Fig. 9b). However, for $R_c/(H_s \xi_{m-1,0})$ greater than 0.60, CV of P_o is far greater than the corresponding CV of q , regardless of the considered N_w . Such a result is due to the fact that mean wave overtopping discharge is a time averaged measurement, thus is less affected by the influence of wave sequence.

Also the variation of q_m and $P_{o,m}$ for increasing N_w was analyzed. The relative percentage error between a generic overtopping descriptor measured after N_w waves (X_{N_w}) and after 1500 waves (X_{1500}) can be calculated as:

$$\epsilon\% = 100 \cdot \frac{X_{1500} - X_{N_w}}{X_{1500}} \quad (6)$$

where X indicates q_m or $P_{o,m}$. From Eq. (6), it follows that $\epsilon\%$ of q_m and $P_{o,m}$ tends to zero for N_w close to 1500. Figs. 9c–d report the

calculated $\epsilon\%$ of q_m and $P_{o,m}$ for increasing N_w , considering the same four representative $R_c/(H_s \xi_{m-1,0})$ used for the analysis of CV . Fig. 9c shows that for $R_c/(H_s \xi_{m-1,0})$ equal to 0.37, 0.50 and 0.62 the absolute value of $\epsilon\%$ of q_m is always lower than 60%. Absolute values of $\epsilon\%$ of q_m smaller than 35% are observed for N_w greater than 500, which is the reference number of waves for overtopping measurement suggested by Romano et al. (2015). If 1000 waves are reproduced as suggested by EurOtop (2018), $\epsilon\%$ of q_m is very small, i.e. 1% for $R_c/(H_s \xi_{m-1,0})$ equal to 0.37 and 0.50 and -10% for $R_c/(H_s \xi_{m-1,0})$ equal to 0.62. For more than 1000 waves, $\epsilon\%$ of q_m is almost constant and close to zero, with some oscillations between $\pm 7\%$ only for the case with $R_c/(H_s \xi_{m-1,0})$ equal to 0.62. The slightly higher variability of $\epsilon\%$ of q_m observed for the third representative $R_c/(H_s \xi_{m-1,0})$ is due to the more significant dependency of wave overtopping phenomena of less energetic sea states on the individual wave characteristics and to the consequent greater uncertainty of the measurements, which has been demonstrated in Section 5.1. Such a dependency is even more evident for $R_c/(H_s \xi_{m-1,0})$ equal to 0.71, which is characterized by an absolute value of $\epsilon\%$ of q_m up to 170%. The error $\epsilon\%$ of q_m is equal to -50% when 1000 waves are reproduced, and it reaches values close to 10% only after about 1300 waves. Such a result is in accordance with the findings discussed in Section 5.1, where CV of the considered wave overtopping measurements (i.e. q^* , P_o and V_{max}) up to 250% was found for $R_c/(H_s \xi_{m-1,0})$ greater than 0.60.

Fig. 9d shows the variation of $\epsilon\%$ of $P_{o,m}$ for increasing N_w . A clear correspondence with the results found for q_m is observed. Absolute values of $\epsilon\%$ for $P_{o,m}$ lower than 50% are reached for N_w equal or greater than 500, when $R_c/(H_s \xi_{m-1,0})$ is equal to 0.37, 0.50 or 0.62. For $R_c/(H_s \xi_{m-1,0})$ equal to 0.37 and 0.50, the absolute value of $\epsilon\%$ for $P_{o,m}$ evaluated after 1000 waves is not higher than 15%. Instead, for $R_c/(H_s \xi_{m-1,0})$ equal to 0.62, $\epsilon\%$ for $P_{o,m}$ ranges between -10% and 10% only after about 1300 waves. Likewise, $\epsilon\%$ for $P_{o,m}$ calculated for $R_c/(H_s \xi_{m-1,0})$ equal to 0.71 is equal to -50% when 1000 waves are considered, and it is close to 10% in absolute value considering about 1300 waves, thus confirming the greater uncertainty that characterizes the measurement of lowest wave overtopping events.

On the basis of the above-discussed results, the investigation on wave overtopping phenomena of damaged and upgraded breakwaters does not need more than 1000 waves, as suggested by EurOtop (2018). Indeed, when longer time series are generated, the uncertainty of the estimation of mean overtopping discharge and probability of overtopping due to the individual wave characteristics does not significantly decrease. Moreover, both q_m and $P_{o,m}$ measured for N_w equal to 1000 and 1500 waves differs by no more than 1% for $R_c/(H_s \xi_{m-1,0})$ lower than 0.60. Such a relative error is close to 50% for $R_c/(H_s \xi_{m-1,0})$ greater than 0.60, because of the more significant effects of wave sequences.

6. Wave overtopping of existing and upgraded structures

In the present section, the hydraulic performances of existing and upgraded breakwaters are assessed in terms of non-dimensional mean wave overtopping discharge, probability of wave overtopping and distribution of the individual wave overtopping volumes. The obtained numerical results are compared to existing state-of-the-art formulas, in order to verify the possibility to use them for the tested non-conventional structures.

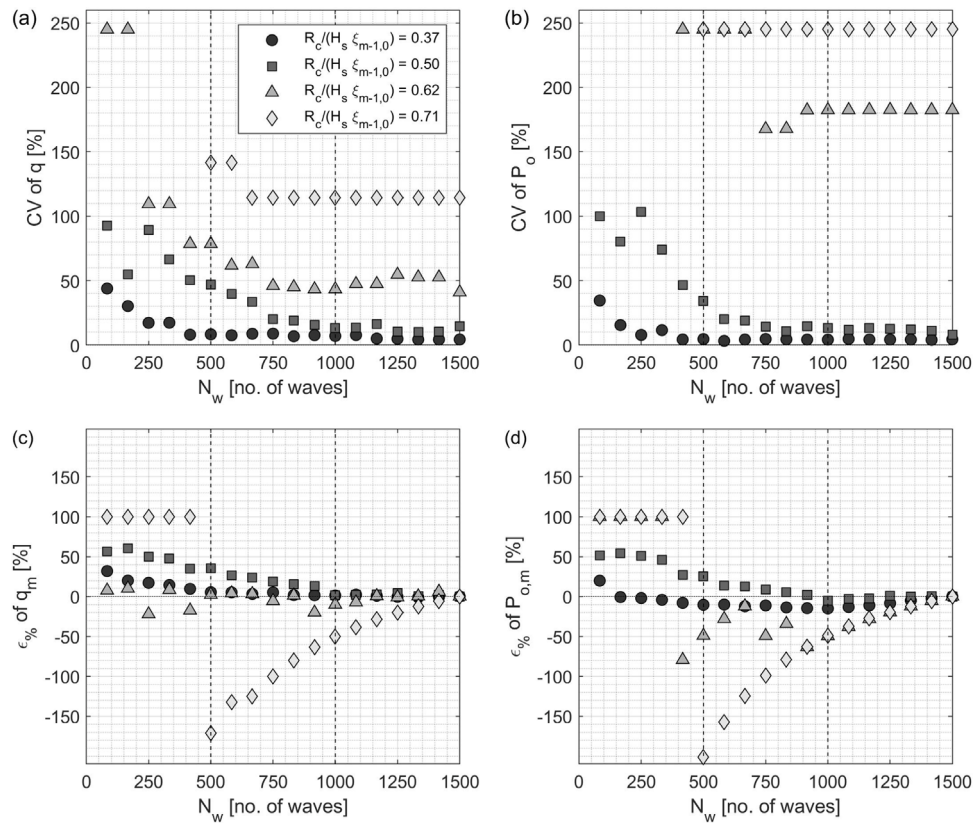


Fig. 9. Coefficient of variation (CV) and mean percentage error ($\epsilon_{\%}$) of the measured numerical (a, c) q and (b, d) P_o as a function of the approximated number of generated waves (N_w) for four representative values of $R_c/(H_s \xi_{m-1,0})$. The dashed vertical lines at N_w equal to 500 and 1000 indicate the reference number of waves suggested by Romano et al. (2015) and EurOtop (2018), respectively.

6.1. Mean wave overtopping discharge

First of all, the hydraulic performances of the tested structures were evaluated in terms of non-dimensional mean wave overtopping discharge. The numerical q^* measured for the existing and upgraded structures were compared with the predictions of the following existing formulas for conventional rubble-mound breakwaters, after verifying that their range of application was consistent with our dataset: (i) the formula proposed by Smolka et al. (2009) for cube- and Cubipod-armored breakwaters; (ii) the formulas developed by Jafari and Etemad-Shahidi (2012) and Etemad-Shahidi and Jafari (2014) using the CLASH dataset (Steendam et al., 2005); (iii) the formula that Molines and Medina (2016) derived from the CLASH Neural Network data (van Gent et al., 2007); (iv) Eq. (5) proposed by EurOtop (2018); (v) the formula proposed by Etemad-Shahidi et al. (2022), which was calibrated on the EurOtop (2018) and Koosheh et al. (2022) databases. The scatter plots in Figs. 10a–e represent such comparisons. In order to quantify the differences between measured and predicted values, the following statistical error indicators were also calculated (see Table 7): (i) the normalized bias NBI of the logarithm of q^* , which gives indications about the average component of the error and assumes a value close to zero for good simulations; (ii) the correlation coefficient r representing the scatter component of the error, which is smaller when r is closer to one; (iii) the symmetrically normalized root mean square error HH (Hanna and Heinold, 1985) of the logarithm of q^* , which combines information about the average and scatter components of the error, with no bias toward simulations that underestimate the average.

Existing prediction formulas considered in Figs. 10a–d produce an overestimation of numerical q^* lower than 10^{-4} , by more than one order of magnitude when the latter is lower than 10^{-5} . Fig. 10e shows predictions that overestimate most of the numerical data, i.e. all values

of numerical q^* smaller than 7×10^{-4} , by more than one order of magnitude when the latter is smaller than 4×10^{-5} . The above-discussed discrepancies between predictions and observations are probably influenced by the significant uncertainty which characterizes the lowest mean wave overtopping discharges (see Section 5), as well as by the expected worse performance of state-of-the-art formulas for q^* lower than the zero-overtopping limit of the experimental tests (see Section 4.3). From a practical point of view, the poor correspondence between predicted and observed q^* lower than the zero-overtopping limit is a minor issue, since the most intense wave overtopping phenomena are of major interest for engineering practices. Figs. 10a–d reveal that for observed q^* higher than 10^{-4} , the considered prediction formulas tend to underestimate the numerical data, up to one order of magnitude. This is likely to be linked to the non-conventional geometry and layering of the tested breakwater configurations. In particular, the irregular shape of the existing armor layer may induce unexpected increase of the wave steepness along the structure slope, thus causing wave breaking for the highest waves, but enabling some of the lowest ones to go beyond the crown wall. The formula proposed by Etemad-Shahidi et al. (2022) gives good predictions only for observed q^* higher than 7×10^{-4} . Table 7 reports the values of NBI , r and HH calculated with reference to the whole available dataset, including also q^* lower than 10^{-5} (i.e. the zero-overtopping limit). It should be noted that the exclusion of values of q^* lower than 10^{-5} would not produce significant variations of the calculated statistical indicators, since they represent only 11% and 12% of the entire dataset for the existing and upgraded structures, respectively. Therefore, even though considering only q^* higher than 10^{-5} may be sufficient for engineering practices, the prediction model performances were assessed considering the entire available dataset to provide a comprehensive evaluation useful also for research purposes. Table 7 shows that the values of NBI , r and HH are quite similar for all the considered prediction formulas. The normalized

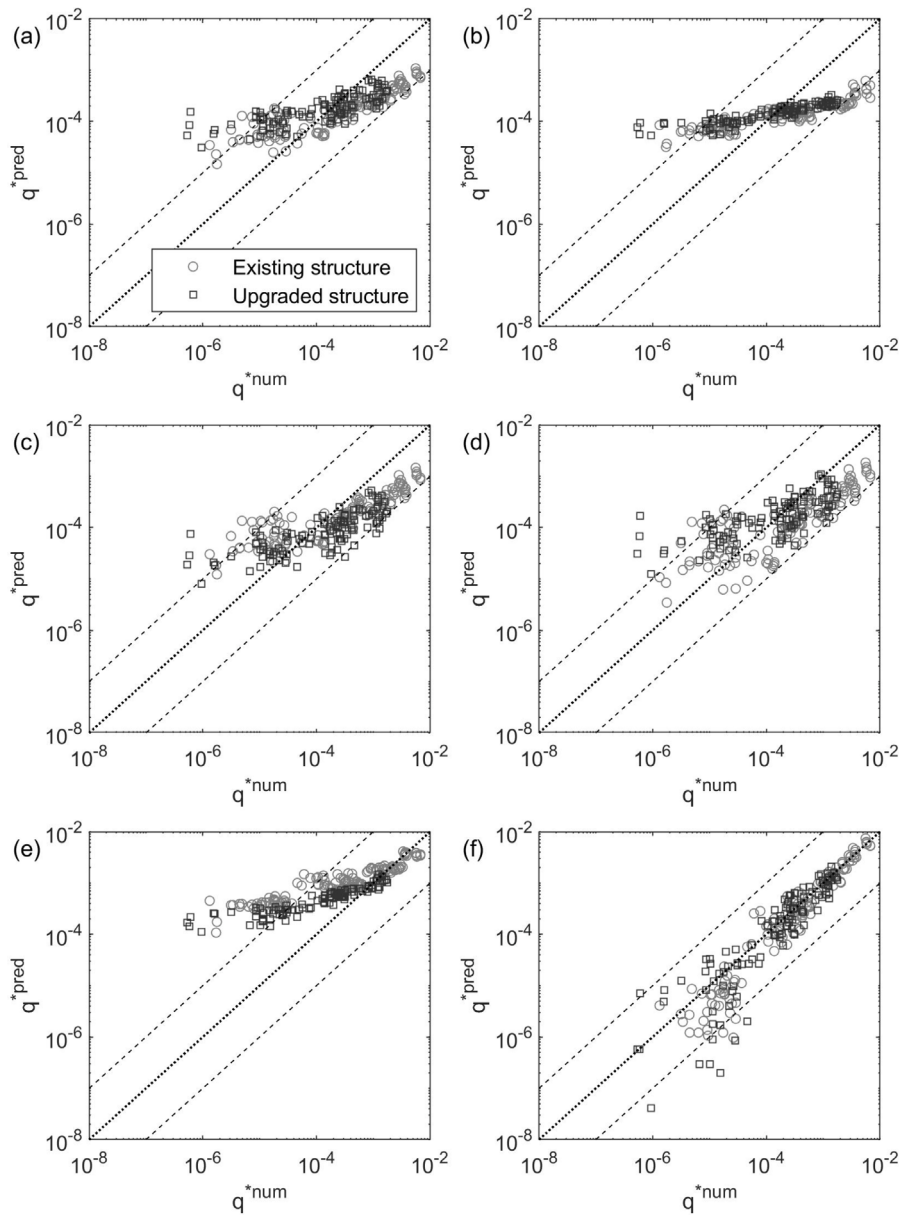


Fig. 10. Comparison between the numerical data on non-dimensional mean wave overtopping discharge and the predictions of the formulas proposed by: (a) Smolka et al. (2009); (b) Jafari and Etemad-Shahidi (2012) and Etemad-Shahidi and Jafari (2014); (c) Molines and Medina (2016); (d) EurOtop (2018); (e) Etemad-Shahidi et al. (2022); (f) Eq. (7). Dashed lines indicate 10 times under/overestimation of the numerical q^* , whereas the dotted line represents the perfect prediction.

Table 7

Statistical indicators of the correspondence between predictions and numerical q^* measured for the existing and upgraded structures.

| Formulation | NBI | | r | | HH | |
|---|----------|----------|----------|----------|----------|----------|
| | Existing | Upgraded | Existing | Upgraded | Existing | Upgraded |
| Smolka et al. (2009) | -0.03 | 0.04 | 0.92 | 0.76 | 0.17 | 0.18 |
| Jafari and Etemad-Shahidi (2012) and Etemad-Shahidi and Jafari (2014) | -0.05 | 0.02 | 0.86 | 0.80 | 0.20 | 0.18 |
| Molines and Medina (2016) | -0.03 | -0.04 | 0.91 | 0.73 | 0.17 | 0.16 |
| EurOtop (2018) | -0.06 | 0.03 | 0.89 | 0.69 | 0.16 | 0.16 |
| Etemad-Shahidi et al. (2022) | 0.18 | 0.16 | 0.89 | 0.89 | 0.28 | 0.24 |
| Eq. (7) | -0.06 | -0.03 | 0.97 | 0.90 | 0.14 | 0.12 |

bias ranges between -0.06 and 0.04 for the formulas employed in Figs. 10a–d, thus indicating a contained average component of the prediction error. This is in accordance with the shape of the data point clouds, of which the first and second halves are placed over and under

the bisector, respectively, thus minimizing the average prediction error. Instead, the formula considered in Fig. 10f produces a more significant averaged overestimation of the observed data. The correlation coefficient is always higher than 0.69 , thus indicating the existence of

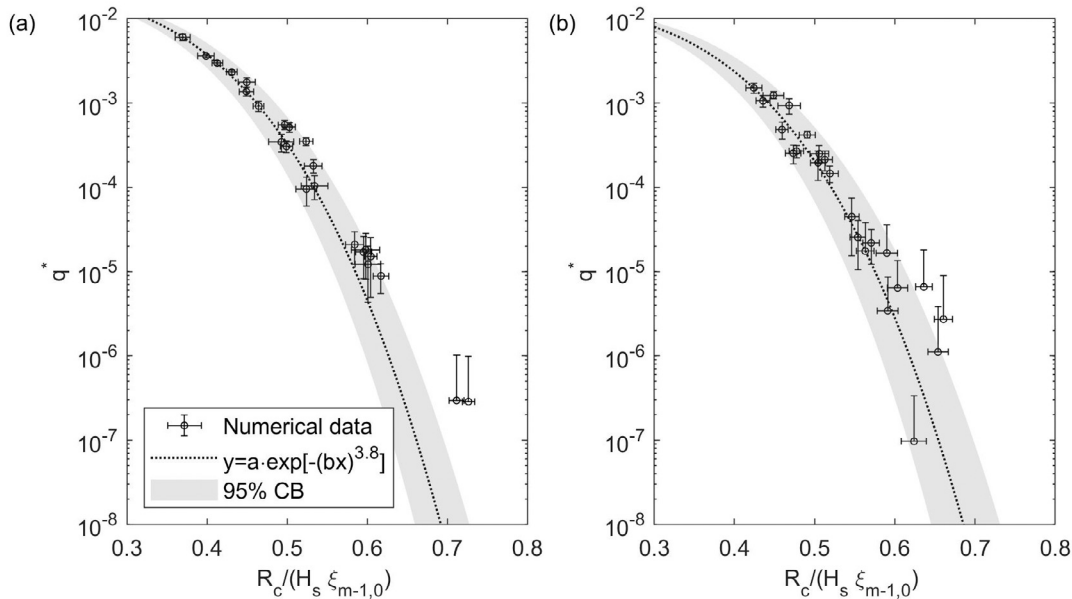


Fig. 11. Site-specific prediction formula fitted to the numerical data on non-dimensional mean wave overtopping discharge as a function of $R_c/(H_s \xi_{m-1,0})$: (a) existing structure; (b) upgraded structure.

Table 8

Coefficients and coefficient of determination of the site-specific equations which describe the relationship between q^* and $R_c/(H_s \xi_{m-1,0})$.

| Structure | c_q | a_q | | b_q | | R^2 |
|-----------|-------|----------|----------|----------|----------|-------|
| | | Estimate | σ | Estimate | σ | |
| Existing | 3.8 | 0.023 | 0.005 | 2.930 | 0.088 | 0.94 |
| Upgraded | 3.8 | 0.015 | 0.006 | 2.933 | 0.112 | 0.78 |

a strong positive relationship between observed and predicted values. Finally, the symmetrically normalized root mean square error ranges between 0.16 and 0.28.

Since none of the tested existing formulas provides an accurate estimate of q^* over the whole investigated range of hydrodynamic conditions, the numerical data on mean wave overtopping discharge were employed for the definition of two site-specific formulas, for the existing and upgraded structures respectively, according to the following format:

$$q^* = \frac{q}{\sqrt{gH_s^3}} = a_q \cdot \exp \left[- \left(b_q \cdot \frac{R_c}{H_s \xi_{m-1,0}} \right)^{c_q} \right] \quad (7)$$

where c_q was calculated as the optimal value for the entire dataset, and a_q and b_q were estimated using the least squares linear regression method. It should be noted that the presence of $\xi_{m-1,0}$, which was used by all the above-mentioned existing formulas with the exception of the one proposed by EurOtop (2018), allows the inclusion of possible breaking phenomena which may develop over the structure slope. Table 8 reports the optimal c_q , the estimate and the standard deviation of a_q and b_q and the corresponding R^2 , calculated for both the existing and upgraded structures. Fig. 11 graphically shows the fitted formulations, which are valid for $10^{-7} < q^* < 10^{-2}$ and $0.30 < R_c/(H_s \xi_{m-1,0}) < 0.80$. The numerical results for each of the reproduced sea states are represented in terms of mean q^* and $R_c/(H_s \xi_{m-1,0})$ evaluated with reference to the six realizations with different seeding, being the vertical and horizontal error bars representative of the corresponding standard deviation. When the lower error bar is absent, it has a negative value, which does not have a physical meaning and cannot be plotted in log-scale. Such a condition occurs when null q^* are recorded for some of the six realizations of a certain sea state.

Fig. 10f shows that the numerical non-dimensional mean overtopping discharge is quite well predicted by the site-specific formulas, also when the lowest and highest q^* are considered. Indeed, the data point cloud is very close to the bisector for the whole range of numerical q^* , though with a more pronounced scatter level for q^* lower than 10^{-5} due to the highest uncertainty of the numerical simulation results (see Section 5). As already stated, the lowest reliability of the predictions for q^* lower than 10^{-5} is of little interest for engineering practices. Table 7 shows that the negative NBI is quite contained, thus indicating a slight tendency of the site-specific formulas to underestimate the observed data on average. The very strong correlation between the numerical and predicted q^* is demonstrated by r equal to or greater than 0.90. Finally, values of HH calculated for the predictions of Eq. (7) are lower than the ones found using state-of-the-art formulas.

6.2. Probability of wave overtopping

The probability of wave overtopping was calculated for both the existing and upgraded structures. The obtained results were compared to the predictions of state-of-the-art formulas developed for conventional rubble-mound breakwaters, whose range of applicability is consistent with our dataset. Two formulas which express P_o as a function of the non-dimensional mean wave overtopping discharge $Q^* = q/(gH_s T_m)$ developed by Besley (1999) and Mares-Nasarre et al. (2020) were considered. Moreover, the following more sophisticated formulation expressing P_o as a function of the sea state characteristics and breakwater geometry was employed (EurOtop, 2018):

$$P_o = \exp \left[- \left(\sqrt{-\ln 0.02} \frac{R_c}{R_{u,2\%}} \right)^2 \right] \quad (8)$$

where $R_{u,2\%}$ is the wave run-up level corresponding to the 2%-value of the hypotized Rayleigh distribution, calculated using the following empirical formula for the case of orthogonal wave attack and neglecting the effects of the toe berm:

$$\frac{R_{u,2\%}}{H_s} = 1.65 \cdot \gamma_f \cdot \xi_{m-1,0} \quad (9)$$

where γ_f is the roughness factor equal to 0.47 for double layer of artificial cubes. Following a similar approach to the one employed for

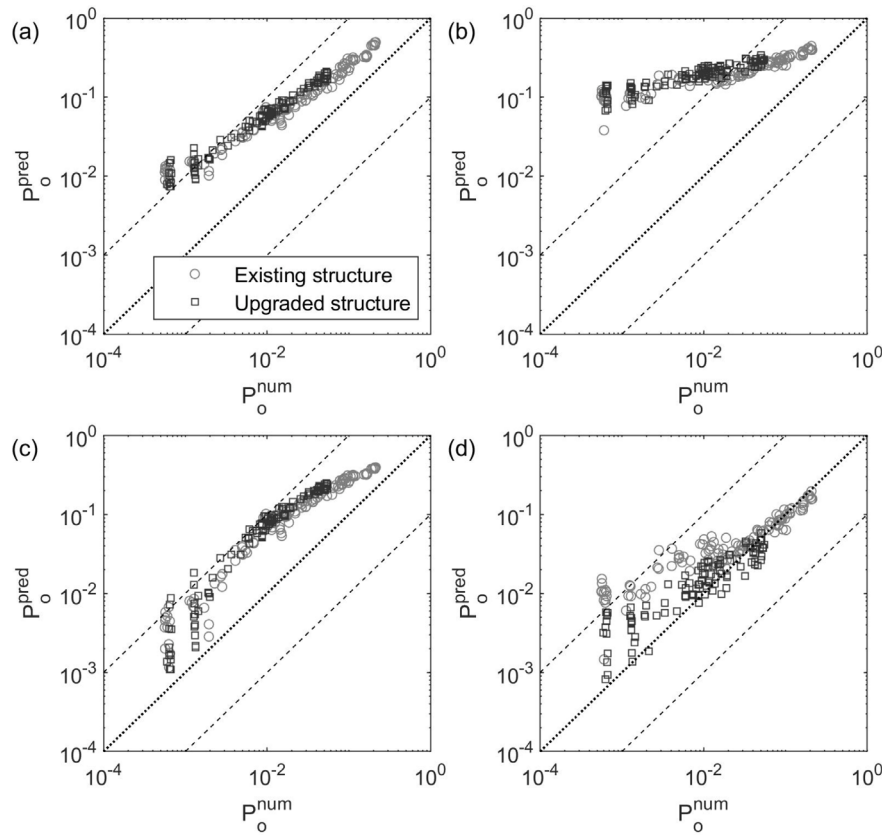


Fig. 12. Comparison between the numerical data on probability of wave overtopping and the predictions of the formulas proposed by: (a) Besley (1999); (b) EurOtop (2018); (c) Mares-Nasarre et al. (2020); (d) Eq. (10). Dashed lines indicate 10 times under/overestimation of the numerical P_o , whereas the dotted line represents the perfect prediction.

Table 9
Statistical indicators of the correspondence between predictions and numerical P_o measured for the existing and upgraded structures.

| Formulation | NBI | | r | | HH | |
|-----------------------------|----------|----------|----------|----------|----------|----------|
| | Existing | Upgraded | Existing | Upgraded | Existing | Upgraded |
| Besley (1999) | 1.77 | 3.57 | 0.97 | 0.97 | 0.95 | 1.54 |
| EurOtop (2018) | 3.90 | 13.44 | 0.88 | 0.84 | 1.44 | 3.07 |
| Mares-Nasarre et al. (2020) | 1.98 | 4.66 | 0.93 | 0.96 | 1.01 | 1.85 |
| Eq. (10) | 0.16 | 0.10 | 0.95 | 0.90 | 0.30 | 0.38 |

the analysis of q^* (see Section 6.1), Fig. 12a–c show the graphical comparison between the observed and predicted probability of overtopping of the existing and upgraded configurations, whereas Table 9 reports the corresponding NBI, r and HH of P_o .

State-of-the-art formulas considered in Figs. 12a–c clearly overestimate the observed probability of wave overtopping. In particular, Fig. 12a–b show predictions higher than the observed probability of wave overtopping by more than one order of magnitude when the latter is lower than 10^{-3} and 2×10^{-2} , respectively. Instead, the existing formula employed in Fig. 12c provides estimates of P_o higher than the observed values by no more than one order of magnitude. The highest scatter level of the data point clouds found for observed P_o lower than 4×10^{-3} is coherent with the uncertainty typical of measurements of overtopping produced by low-energy sea states (see Section 5.1). Table 9 shows that the positive NBI ranges between 1.77 and 13.44, thus confirming the tendency of state-of-the-art formulas to return predictions of P_o higher than the observed ones. The correlation among predicted and observed values is very strong, with r in the range 0.84–0.97. Finally, HH assumes values between 0.95 and 3.07.

The peculiar geometry and layering of the tested rubble-mound structures are likely to contribute to the deviation of the observed probability of wave overtopping from the predictions of existing formulas. In particular, breaking phenomena along the irregular slope of

the existing armor layer and the increased porosity of the structure with additional blocks may induce the reduction of the number of overtopped waves with respect to state-of-the-art predictions. Such a reduction does not necessarily corresponds to values of q^* lower than the expected ones, because the mean wave overtopping discharge is influenced not only by the number of overtopped waves, but also by their energy content. In any case, concerning the prediction formulation proposed by EurOtop (2018), a certain overestimation of the measured number of overtopping waves is expected, because Eqs. (8) and (9) refer to the run-up level on a straight rock armored slope. Indeed, as explained by Schüttrumpf et al. (2018), wave overtopping discharge is not measured in the correspondence of the run-up level, but some onshore distance away, in this case behind the crown wall.

A more reliable description of the probability of wave overtopping for a certain structure type can be obtained by adapting traditional formulations to specific experimental data. To this aim, Eqs. (8) and (9) can be combined and rewritten as:

$$P_o = exp \left[- \left(c_{P_o} \frac{R_c}{H_s \xi_{m-1,0}} \right)^2 \right] \quad (10)$$

where c_{P_o} is an empirical coefficient that includes the peculiarities of the considered structure. For instance, Victor et al. (2012) proposed a relationship for the calculation of c_{P_o} as a function of the slope

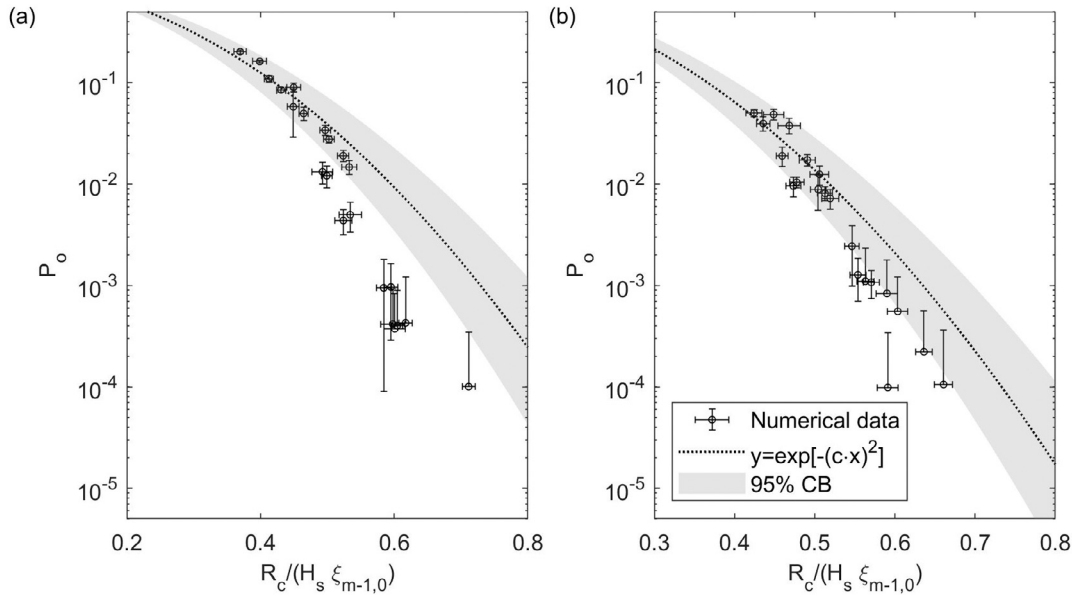


Fig. 13. Site-specific prediction formula fitted to the numerical data on probability of wave overtopping expressed as function of $R_c/(H_s \xi_{m-1,0})$: (a) existing structure; (b) upgraded structure.

Table 10

Coefficients and coefficient of determination of the site-specific equations which describe the relationship between P_o and $R_c/(H_s \xi_{m-1,0})$.

| Structure | c_{p_o} | | R^2 |
|-----------|-----------|----------|-------|
| | Estimate | σ | |
| Existing | 3.604 | 0.221 | 0.88 |
| Upgraded | 4.140 | 0.227 | 0.76 |

angle, specific for smooth slopes and neglecting the effect of $T_{m-1,0}$ included in Eq. (10). Likewise, Iuppa et al. (2019) defined a formula for the calculation of c_{p_o} specific for OBREC systems with a 2:3 seaside slope, not considering the influence of $\xi_{m-1,0}$ on wave overtopping phenomena. In the present work, two site-specific formulas were defined, by fitting the coefficient c_{p_o} of Eq. (10) to our data. The proposed formulation for the existing and upgraded cube-armored breakwaters includes the effects of the wave steepness, which is expressed by $\xi_{m-1,0}$. Moreover, the empirical coefficient c_{p_o} allows to take into account the geometrical irregularities of the existing armor slope, which are likely to induce the rise of the wave steepness and wave breaking of the highest waves, as well as the unusually large thickness of the porous media composed by the layers of the upgraded breakwater, which is likely to cause significant wave energy dissipation. Table 10 reports the estimated c_{p_o} and its standard deviation, together with the R^2 of the fitting performed through the least squares method. Moreover, Fig. 13 shows the numerical dataset and the fitted curves with the corresponding 95% confidence bounds. According to the procedure employed for the visualization of the mean wave overtopping discharge data, the mean value and the standard deviation of P_o were calculated for each simulated sea state, considering six realizations.

Fig. 12d shows that the site-specific formulas provide a good estimate of the observed P_o when the latter is higher than 10^{-2} . The highest scatter level which characterizes the data point cloud for observed P_o lower than 10^{-2} is again due to the significant level of uncertainty which affects the measurement of the less intense wave overtopping events (see Section 5). In any case, the overestimation of the numerical P_o is never higher than one order of magnitude. Table 9 reveals that the fitted Eq. (10) produces predictions with *NBI* and *HH* much lower

than the considered state-of-the-art formulas. Moreover, the correlation between observed and estimated P_o is always strong, being r equal to 0.95 and 0.90 for the case of existing and upgraded structures, respectively.

6.3. Overtopping volume distribution

The statistical analysis of wave overtopping phenomena consisted in the calculation of the probability density function of the individual wave overtopping volumes for each simulated sea state, considering both the existing and the upgraded structure. The distribution of individual wave overtopping volumes is generally well-described by the two-parameter Weibull distribution (EurOtop, 2018):

$$P_{V_i}(V) = P[V_i > V] = \exp\left[-\left(\frac{V}{a_V}\right)^{b_V}\right] \quad (11)$$

where P_{V_i} is the probability that the generic individual volume V_i is greater than the reference value V , and a_V and b_V are the scale and shape parameter of the distribution, respectively. Here, the Weibull distribution was adapted to the sample of individual volumes of each simulation using the maximum likelihood estimation method, and its goodness of fit was verified through the Kolmogorov–Smirnov test at the 5% significance level. Following the work of Bruce et al. (2009), the adaptation of the Weibull distribution was not performed for simulations giving less than 15 overtopping events, which are characterized by very low mean wave overtopping discharge. In this regard, Fig. 14 shows the number of overtopping waves and the corresponding non-dimensional mean overtopping discharge for the 300 run cases. The variation of q^* with increasing N_o (i.e. P_o) is well described by a linear relationship in the form $y = C \cdot x$. Table 11 reports the estimate and the upper and lower *CB* of the coefficient C , together with the R^2 of the fitting performed through the least squares method. For N_o less than or equal to 15, q^* is lower than 4×10^{-5} , which means that *CV* of P_o ranges between 50% and 250% (see Section 5). Therefore, the Weibull distribution described by Eq. (11) was adapted only to the individual overtopping volumes recorded during the simulations characterized by *CV* of P_o not greater than 50%. For instance, Fig. 15 shows the empirical and fitted cumulative distribution function (CDF) calculated for a high energy sea state in the presence of the existing structure, and

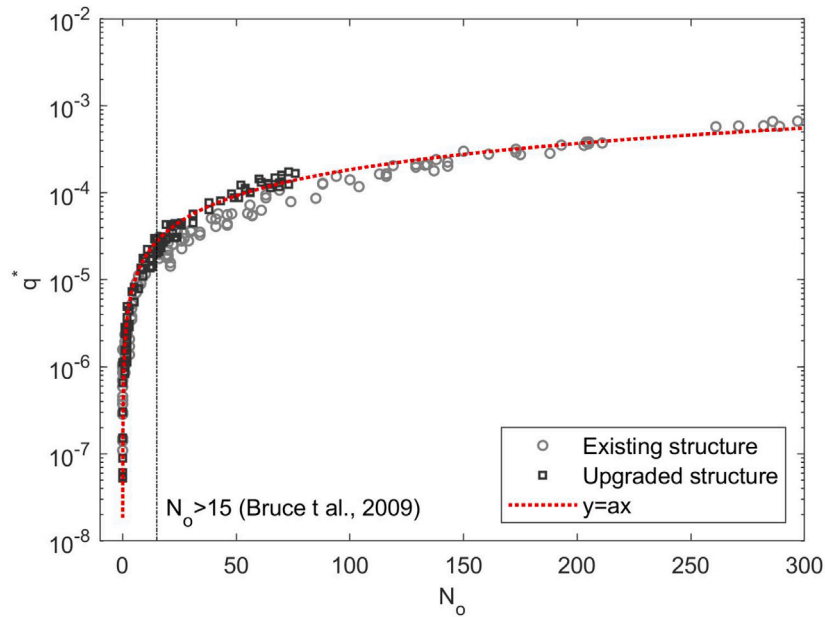


Fig. 14. Non-dimensional mean overtopping discharge expressed as a function of the number of overtopping waves (i.e. of individual overtopping volumes).

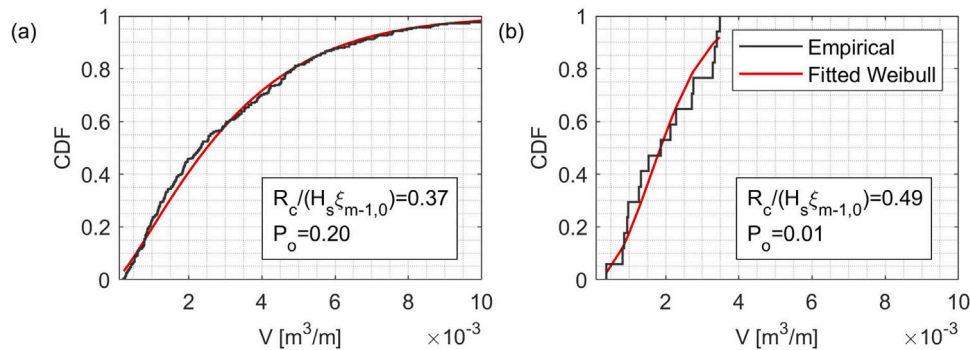


Fig. 15. Cumulative distribution functions adapted to the individual overtopping volumes measured during two representative simulations carried out for the (a) existing and (b) upgraded structures.

Table 11
Coefficient and coefficient of determination of the linear relationship between N_o and q^* .

| Law | C | | | R^2 |
|-------------|------------------------|------------------------|------------------------|-------|
| | Estimate | 95% $C_{B_{up}}$ | 95% $C_{B_{low}}$ | |
| $N_o - q^*$ | 1.845×10^{-6} | 1.803×10^{-6} | 1.887×10^{-6} | 0.96 |

for a low energy one in the presence of the upgraded breakwater. The poorest correspondence between the data and the fitted Weibull distribution, which is often observed for the lowest V , does not influence the analysis of the more interesting largest overtopping volumes (Zanutigh et al., 2014). Moreover, the results of the Kolmogorov–Smirnov test were positive for all the considered samples.

The calculated shape and scale parameters of the Weibull distributions were compared to the predictions of state-of-the-art formulas. In particular, the shape parameter for conventional rubble-mound structures can be evaluated as a function of the ratio $q/(gH_s T_{m-1,0})$, using the following empirical formula (Zanutigh et al., 2014) as suggested by EurOtop (2018):

$$b_V = 0.85 + 1500 \cdot \left(\frac{q}{gH_s T_{m-1,0}} \right)^{1.3} \quad (12)$$

Fig. 16 compares the estimates of b_V measured with the existing and upgraded structures using Eq. (12). In order to link each b_V to the corresponding probability of wave overtopping, a color scale is employed. The scatter of the data decreases for increasing P_o or $q/(gH_s T_{m-1,0})$. Such a result agree with the fact that for small wave overtopping events the measurement dispersion of is higher (see Section 5). The calculated values of b_V , which correspond to $q/(gH_s T_{m-1,0})$ ranging between 1×10^{-5} and 5×10^{-4} , seem to be significantly underestimated by Eq. (12). However, our dataset is similar to the highest scattered part of the CLASH rubble-mound dataset (Steendam et al., 2005) used by Zanutigh et al. (2014) for the calibration of Eq. (12). In particular, the region characterized by P_o lower than 0.05 and b_V greater than 1.40 is not included into the empirical model. Fig. 17 demonstrates that a great part of the calculated couples $P_o - b_V$ follows into such a range, and hence they are reasonably not described by the formula of Zanutigh et al. (2014). Also the values of b_V with P_o higher than 0.05, which were found for the existing structure, are almost overlapping the clash rubble-mound dataset. The same holds for the couples $P_o - b_V$ with P_o lower than 0.05 and b_V lower than 1.40. The similarity between the shape parameters evaluated for the existing and the upgraded structure and the ones calculated for the clash rubble-mound dataset is in accordance with the findings of Bruce et al. (2009) and Zanutigh et al. (2014), who verified that b_V is not significantly

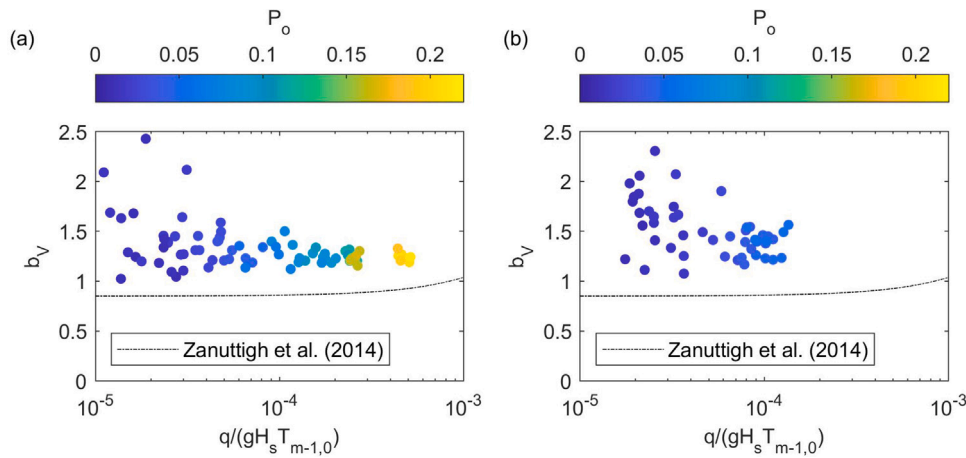


Fig. 16. Comparison between the values of the shape parameter of the Weibull distributions fitted to the numerical data expressed as a function of $q/(gH_s T_{m-1,0})$ and the predictions of Zanuttigh et al. (2014).

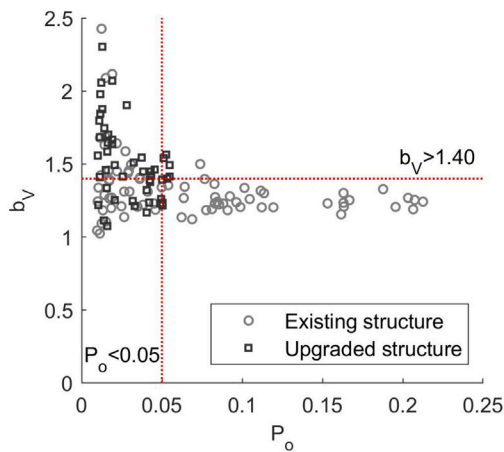


Fig. 17. Shape parameter of the Weibull distribution of the individual wave overtopping volumes expressed as a function of the probability of wave overtopping. The data with $P_o < 0.05$ and $b_V > 1.40$ belong to the region not considered in the formulation of Zanuttigh et al. (2014).

influenced by the armor layer surface roughness, the structure porosity and the number of layers of armor blocks (i.e. one or two layers) for the range of $q/(gH_s T_{m-1,0})$ considered here. New site-specific formulas to estimate b_V were not defined because of the too high scattered nature of the dataset.

The scale parameter of the Weibull distribution can be estimated using the following relationship (EurOtop, 2018):

$$a_V = \frac{1}{\Gamma\left(1 + \frac{1}{b_V}\right)} \cdot \frac{qT_m}{P_o} \quad (13)$$

where Γ is the gamma function. In the present work, q , T_m , P_o are the output of the numerical simulations. The shape parameter b_V should be calculated using Eq. (12). However, as already discussed, such a formula is not sufficiently reliable for the range of $q/(gH_s T_{m-1,0})$ considered here. Therefore, the estimated b_V were employed, to verify the adequacy of Eq. (13) in predicting the correspondent a_V . Following the same approach employed in Sections 6.1 and 6.2, Figs. 18a–b show the scatter plot for the comparison between the numerical and the predicted scale parameter, using a color scale to relate each data point to the corresponding measured P_o . Moreover, the statistical error indicators NBI , r and HH were calculated to quantify the differences between measured and predicted values.

The obtained results show that Eq. (13) produces a quite good prediction of the observed a_V , being r greater than 0.90 and HH not higher than 0.21, for both the tested configurations. However, the employed formulation tends to slightly overestimate the numerical a_V , as demonstrated by the position of the data point clouds with respect to the bisector, and also by the positive NBI equal to 0.10 and 0.23 for the existing and upgraded structures, respectively.

If the Weibull distribution of individual wave overtopping volumes is known, the expected maximum V_{max} can be calculated using the following formula (EurOtop, 2018):

$$V_{max} = a_V \cdot [\ln(N_o)]^{1/b_V} \quad (14)$$

Figs. 18c–d show the comparison between the observed and predicted V_{max} , using again the scatter plot with color scale to relate each data point to the corresponding P_o . The statistical error indicators NBI , r and HH were also calculated. The prediction formula tends to slightly underestimate the measured maximum wave overtopping volumes. Such a result is confirmed by the values of NBI , which is equal to -0.13 and -0.14 for the existing and upgraded structures, respectively. However, the correlation coefficient is close to 0.90 and the parameter HH is about 0.20 for both the tested configurations. Therefore, despite of the considered non-conventional configurations, Eq. (14) is able to provide a quite good prediction of the maximum wave overtopping volume produced during a single event. Such a result confirms that the traditional formulation for the statistical characterization of the individual wave overtopping volumes, which is based on the use of the Weibull distribution, seems adequate also for damaged or upgraded rubble-mound breakwaters when P_o ranges between 5.6×10^{-4} and 2.1×10^{-1} .

7. Conclusions

Nowadays, a huge number of historical harbor rubble-mound breakwaters appears severely damaged and needs to be upgraded. A thorough comprehension of the wave overtopping phenomena of existing and upgraded structures is fundamental to design upgrading options able to ensure safety for port operations. However, actual manuals and guidelines propose only design and prediction formulas calibrated for newly built breakwaters, which may not adequately describe the response of damaged or upgraded structures with irregular armor slope and/or unusual layering. Here, for the first time, two-dimensional numerical simulations of the wave–structure interaction were performed considering damaged and upgraded cube-armored rubble-mound breakwaters. The model *IH2VOF*, which has been already applied to study non-conventional structures, was successfully calibrated using the values of reflection coefficient and mean wave

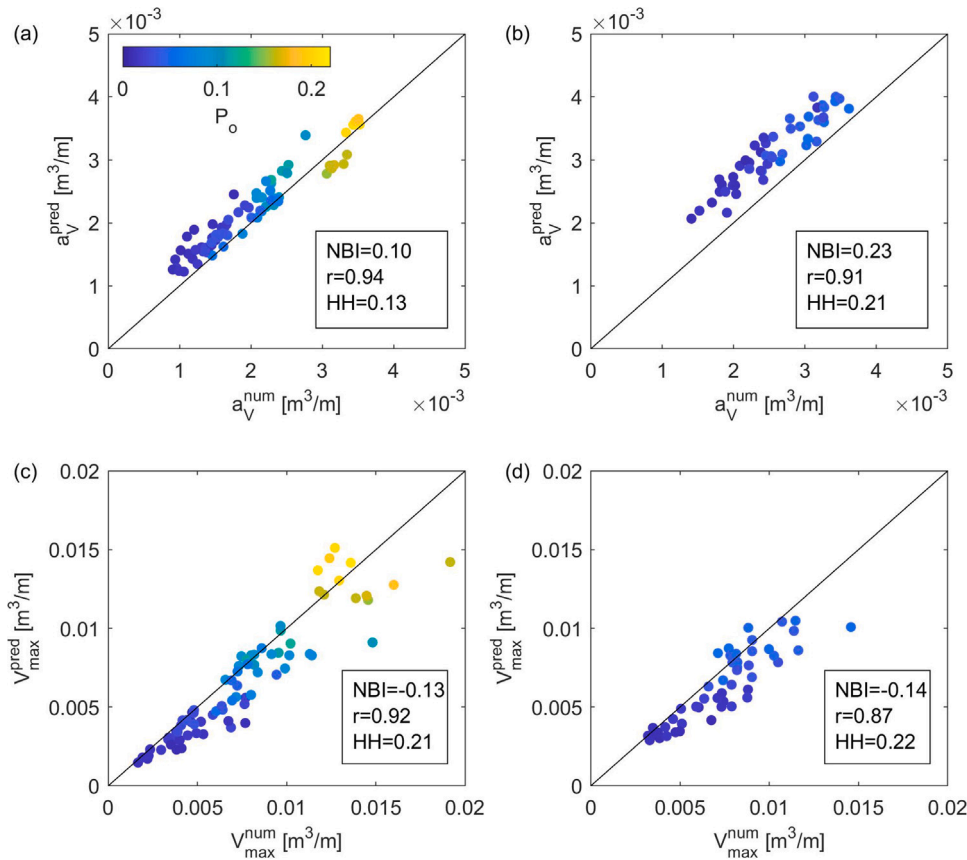


Fig. 18. Comparison between the fitted and estimated distributions of individual wave overtopping volumes according to EurOtop (2018): scale parameter of the Weibull distribution for the (a) existing and (b) upgraded structures; maximum wave overtopping volume for the (c) existing and (d) upgraded structures.

overtopping discharge acquired during the experimental campaign previously carried out at the Hydraulic Laboratory of the University of Catania. Data from 300 simulations were employed to perform two kinds of analysis: (i) the assessment of the effects of wave series sequence and length on the uncertainty of the overtopping measurements; (ii) the comparison between the obtained overtopping data and the predictions of state-of-the-art formulations calibrated only for newly built structures.

In accordance with existing literature, present results reveal that also for the non-conventional tested structures the effects of wave sequence, which was characterized by the parameter H_{max}/H_s ranging between 1.66 and 2.00, produce higher uncertainty in the estimation of q^* , P_o and V_{max} for less energetic sea states, following an exponential law. In order to keep CV of the above-mentioned quantities below 50%, only sea states with $R_c/(H_s \xi_{m-1,0})$ lower than 0.50 should be considered, which correspond to q^* greater than 10^{-4} . The number of waves contributes to the reduction of CV , to a greater extent for small $R_c/(H_s \xi_{m-1,0})$. In particular, for each simulated wave condition, CV of q and P_o reaches a certain stability only after 750 waves. For $R_c/(H_s \xi_{m-1,0})$ lower than 0.60, no more than 1000 waves are required to investigate the wave overtopping phenomena, as suggested by EurOtop (2018) with reference to conventional rubble-mound breakwaters. Indeed, the percentage error between the estimated mean q and P_o after 1000 and 1500 waves is smaller than 1%. Instead, for the less energetic sea states (i.e. $R_c/(H_s \xi_{m-1,0})$ greater than 0.60), which produce wave overtopping processes more influenced by wave sequence, CV of P_o is up to 3.5 times greater than the corresponding CV of the averaged quantity q , regardless of wave series length. Moreover, the mean values of q and P_o evaluated after 1000 and 1500 waves differ by about 50%.

Wave overtopping data acquired after 1500 waves were compared to the predictions of state-of-the-art formulations developed for conventional rubble-mound breakwaters. Existing formulas for the estimation

of the non-dimensional mean wave overtopping discharge tend to overestimate q^* lower than 10^{-4} , in some cases by more than one order of magnitude. It should be mentioned that the prediction of q^* lower than 10^{-5} , i.e. the zero-overtopping limit suggested by EurOtop (2018), is a minor issue for engineering practices. On the contrary, the highest q^* are generally underestimated, by one order of magnitude at most. The inability of existing formulas to capture the hydraulic response of the tested configurations is likely due to technical limits of the experimental acquisitions employed to calibrate them, as well as to the irregular shape of the damaged armor layer, which may cause the increase of the wave steepness during propagation over the breakwater, and the non-conventional layering of the upgraded structure. In order to take into account the effects of such features, a new site-specific formula that includes the effects of the slope angle and of $T_{m-1,0}$ was defined, for $0.30 < R_c/(H_s \xi_{m-1,0}) < 0.80$ and $10^{-7} < q^* < 10^{-2}$, distinguishing between damaged and upgraded breakwaters. Concerning the probability of wave overtopping, all the considered existing prediction formulas overestimate P_o of the tested non-conventional structures. Therefore, the traditional formula for the prediction of P_o based on the wave run-up height as a function of $\xi_{m-1,0}$ suggested by EurOtop (2018) was adapted to the numerical data, through the calculation of the empirical coefficient c_{p_o} to include the effects of the armor slope irregularities of the existing structure, and of the greater porosity of the upgraded breakwater. Finally, the traditional approach for the statistical characterization of the individual wave overtopping volumes and the calculation of V_{max} appeared adequate also for damaged or upgraded rubble-mound breakwaters, for the considered range of P_o (i.e. $5.6 \times 10^{-4} < P_o < 2.1 \times 10^{-1}$). A two-parameter Weibull probability density function properly represents the individual wave overtopping volumes distribution of the damaged and upgraded breakwaters, and the estimated values of the shape parameter are similar to the ones

calculated by Zanuttigh et al. (2014) for the CLASH dataset (Steendam et al., 2005) for $q/(gH_s T_{m-1,0})$ lower than 10^{-3} . Moreover, existing formulas for the calculation of the scale parameter and of V_{max} (EurOtop, 2018) provide good predictions of the numerical values, with normalized bias not higher than 0.25, correlation coefficients not lower than 0.87 and normalized root mean square error between 0.13 and 0.21.

The obtained results highlighted that existing prediction formulas, which were only calibrated for newly built rubble-mound breakwaters, may be not suitable for the design of upgrading solutions of historical breakwaters. Indeed, state-of-the-art formulas for the prediction of the non-dimensional mean wave overtopping discharge produce q^* up to 300 times higher and 0.9 lower than the observed values for sea states characterized by $R_c/H_s > 1.70$ and $R_c/H_s < 1.30$, respectively. Moreover, traditional formulations for the evaluation of the probability of wave overtopping may provide values of P_o more than 200 times larger than the observed ones. Therefore, it is essential to use an ad-hoc prediction tool for the assessment of the hydraulic performances of damaged and upgraded structures. CFD models are affected by intrinsic limits in reproducing wave transformation processes and the interaction between waves and porous structures, which are essentially linked to the required computational power and to the necessity to introduce some simplifications for the formulation of the problem. In this regard, the volume-averaged approach employed for the definition of the VARANS equations requires the calibration of several porous media flow parameters based on experimental data, which implies the increase of economic and time costs of the modeling phase. Nevertheless, the proposed methodology for the setup of an especially calibrated numerical model appears as an efficient and effective method to reduce uncertainties in the assessment of the damaged and upgraded structure hydraulic behavior, which would influence design features, reliability and costs of the upgrading solutions. Experimental data on wave reflection and overtopping of the existing and upgraded breakwaters are needed to calibrate the selected two-dimensional CFD numerical model, which then can be employed to run a huge number of simulations with limited computational costs. The numerical dataset is employed to define site-specific wave overtopping prediction formulas, to be used during the design phase, preferably following a probabilistic approach (Stagnitti et al., 2022, 2023a).

The present work also contributes to the development of a large dataset to be used for the calibration of widely usable wave overtopping prediction formulas for damaged and upgraded rubble-mound breakwaters, which do not exist yet. Further simulations should be performed to consider different geometries and layering. Moreover, the effects of more intense wave overtopping events (i.e. with $P_o > 0.20$) should be further investigated, in order to allow a complete comparison with data on individual wave overtopping volume distributions of conventional structures.

CRedit authorship contribution statement

M. Stagnitti: Methodology, Investigation, Validation, Formal analysis, Writing – original draft. **J.L. Lara:** Conceptualization, Methodology, Validation, Formal analysis, Writing – review & editing, Supervision. **R.E. Musumeci:** Conceptualization, Methodology, Writing – review & editing, Supervision. **E. Foti:** Conceptualization, Writing – review & editing, Supervision.

Declaration of competing interest

The authors declare that they have no known competing financial interests or personal relationships that could have appeared to influence the work reported in this paper.

Data availability

Data will be made available on request.

Acknowledgments

This work has been funded by: the projects Interazione Moto Ondoso - Strutture (IMOS) and VARIO - VALutazione del Rischio Idraulico in sistemi cOmplexi of the University of Catania; the Horizon 2020 European Union Funding for Research & Innovation project REST COAST; the PNR 2015–2020 project ISYPORT.

References

- Besley, P., 1999. Overtopping of seawalls. Environment Agency.
- Bruce, T., Van der Meer, J., Franco, L., Pearson, J., 2009. Overtopping performance of different armour units for rubble mound breakwaters. *Coast. Eng.* 56, 166–179.
- Burcharth, H.F., Andersen, T.L., Lara, J.L., 2014. Upgrade of coastal defence structures against increased loadings caused by climate change: A first methodological approach. *Coast. Eng.* 87, 112–121.
- Chorin, A.J., 1968. Numerical solution of the Navier-Stokes equations. *Math. Comp.* 22, 745–762.
- Chorin, A.J., 1969. On the convergence of discrete approximations to the Navier-Stokes equations. *Math. Comp.* 23, 341–353.
- Di Lauro, E., Lara, J.L., Maza, M., Losada, I.J., Contestabile, P., Vicinanza, D., 2019. Stability analysis of a non-conventional breakwater for wave energy conversion. *Coast. Eng.* 145, 36–52.
- Di Lauro, E., Maza, M., Lara, J.L., Losada, I.J., Contestabile, P., Vicinanza, D., 2020. Advantages of an innovative vertical breakwater with an overtopping wave energy converter. *Coast. Eng.* 159, 103713.
- Etamad-Shahidi, A., Jafari, E., 2014. New formulae for prediction of wave overtopping at inclined structures with smooth impermeable surface. *Ocean Eng.* 84, 124–132.
- Etamad-Shahidi, A., Koosheh, A., van Gent, M.R., 2022. On the mean overtopping rate of rubble mound structures. *Coast. Eng.* 177, 104150.
- EurOtop, 2018. Manual on Wave Overtopping of Sea Defences and Related Structures. an Overtopping Manual Largely Based on European Research, But for Worldwide Application.
- Faraci, C., Scandura, P., Foti, E., 2015. Reflection of sea waves by combined caissons. *J. Waterw. Port Coast. Ocean Eng.* 141, 04014036.
- Foti, E., Musumeci, R.E., Stagnitti, M., 2020. Coastal defence techniques and climate change: a review. *Rendiconti Lincei. Scienze Fisiche E Naturali* 31, 123–138.
- Franco, L., 1994. Vertical breakwaters: the Italian experience. *Coast. Eng.* 22, 31–55.
- Garcia, N., Lara, J., Losada, I., 2004. 2-D numerical analysis of near-field flow at low-crested permeable breakwaters. *Coast. Eng.* 51, 991–1020.
- Guanche, R., Losada, I.J., Lara, J.L., 2009. Numerical analysis of wave loads for coastal structure stability. *Coast. Eng.* 56, 543–558.
- Hanna, S.R., Heinold, D.W., 1985. Development and Application of a Simple Method for Evaluating Air Quality Models, 4409. American Petroleum Institute.
- Hughes, S.A., 2014. Coastal engineering challenges in a changing world. *J. Appl. Water Eng. Res.* 2, 72–80.
- Iuppa, C., Cavallaro, L., Musumeci, R.E., Vicinanza, D., Foti, E., 2019. Empirical overtopping volume statistics at an OBREC. *Coast. Eng.* 152, 103524.
- Jafari, E., Etamad-Shahidi, A., 2012. Derivation of a new model for prediction of wave overtopping at rubble mound structures. *J. Waterw. Port Coast. Ocean Eng.* 138, 42–52.
- Jensen, O.J., Bisgaard, A., Wood, H., Genovese, N., 2018. Alderney breakwater, a developed rehabilitation solution. In: *Coasts, Marine Structures and Breakwaters 2017: Realising the Potential*. ICE Publishing, pp. 575–585.
- Koosheh, A., Etamad-Shahidi, A., Cartwright, N., Tomlinson, R., van Gent, M.R., 2021. Individual wave overtopping at coastal structures: A critical review and the existing challenges. *Appl. Ocean Res.* 106, 102476.
- Koosheh, A., Etamad-Shahidi, A., Cartwright, N., Tomlinson, R., van Gent, M.R., 2022. Experimental study of wave overtopping at rubble mound seawalls. *Coast. Eng.* 172, 104062.
- Lara, J., Garcia, N., Losada, I., 2006. RANS modelling applied to random wave interaction with submerged permeable structures. *Coast. Eng.* 53, 395–417.
- Lara, J.L., Losada, I.J., Guanache, R., 2008. Wave interaction with low-mound breakwaters using a RANS model. *Ocean Eng.* 35, 1388–1400.
- Lara, J.L., Losada, I.J., Maza, M., Guanache, R., 2011a. Breaking solitary wave evolution over a porous underwater step. *Coast. Eng.* 58, 837–850.
- Lara, J.L., Lucio, D., Tomas, A., Di Paolo, B., Losada, I.J., 2019. High-resolution time-dependent probabilistic assessment of the hydraulic performance for historic coastal structures: application to Lúcar Breakwater. *Phil. Trans. R. Soc. A* 377, 20190016.
- Lara, J.L., Ruju, A., Losada, I.J., 2011b. Reynolds averaged Navier–Stokes modelling of long waves induced by a transient wave group on a beach. *Proc. R. Soc. A* 467, 1215–1242.
- Lin, P., 1998. Numerical Modeling of Breaking Waves. Cornell University.
- Liu, P.L.-F., Lin, P., Chang, K.-A., Sakakiyama, T., 1999. Numerical modeling of wave interaction with porous structures. *J. Waterw. Port Coast. Ocean Eng.* 125, 322–330.
- Losada, I.J., Lara, J.L., Christensen, E.D., Garcia, N., 2005. Modelling of velocity and turbulence fields around and within low-crested rubble-mound breakwaters. *Coast. Eng.* 52, 887–913.

- Losada, I.J., Lara, J.L., Guanche, R., Gonzalez-Ondina, J.M., 2008. Numerical analysis of wave overtopping of rubble mound breakwaters. *Coast. Eng.* 55, 47–62.
- Losada, I.J., Lara, J.L., del Jesus, M., 2016. Modeling the interaction of water waves with porous coastal structures. *J. Waterw. Port Coast. Ocean Eng.* 142, 03116003.
- Mares-Nasarre, P., Molines, J., Gomez-Martin, M.E., Medina, J.R., 2020. Individual wave overtopping volumes on mound breakwaters in breaking wave conditions and gentle sea bottoms. *Coast. Eng.* 159, 103703.
- Massie, W.W., 1976. *Coastal Engineering*. Vol. III: Breakwater Design. TU Delft, Section Hydraulic Engineering.
- Mata, M.L., van Gent, M.R., 2023. Numerical modelling of wave overtopping discharges at rubble mound breakwaters using OpenFOAM®. *Coast. Eng.* 181, 104274.
- McCabe, M., Stansby, P., Apsley, D., 2013. Random wave runup and overtopping a steep sea wall: Shallow-water and Boussinesq modelling with generalised breaking and wall impact algorithms validated against laboratory and field measurements. *Coast. Eng.* 74, 33–49.
- Molines, J., Medina, J.R., 2016. Explicit wave-overtopping formula for mound breakwaters with crown walls using CLASH neural network-derived data. *J. Waterw. Port Coast. Ocean Eng.* 142, 04015024.
- Oumeraci, H., 1994. Review and analysis of vertical breakwater failures - lessons learned. *Coast. Eng.* 22, 3–29.
- Pearson, J., Bruce, T., Allsop, W., 2002. Prediction of wave overtopping at steep seawalls—variabilities and uncertainties. In: *Ocean Wave Measurement and Analysis*, 2001. pp. 1797–1808.
- Reis, M.T., Neves, M.G., Lopes, M.R., Hu, K., Silva, L.G., 2011. Rehabilitation of Sines west breakwater: wave overtopping study. In: *Proceedings of the Institution of Civil Engineers-Maritime Engineering*, vol. 164. Thomas Telford Ltd, pp. 15–32.
- Rodi, W., 1993. *Turbulence Models and their Application in Hydraulics*. CRC Press.
- Romano, A., Bellotti, G., Briganti, R., Franco, L., 2015. Uncertainties in the physical modelling of the wave overtopping over a rubble mound breakwater: The role of the seeding number and of the test duration. *Coast. Eng.* 103, 15–21.
- Santos-Ferreira, A., Cabral, M., Santos, C., 2015. The rehabilitation of north breakwater of Nazaré harbor, Portugal. *Procedia Eng.* 116, 755–762.
- Schüttrumpf, H., van der Meer, J., Kortenhaus, A., Bruce, T., Franco, L., 2018. Wave run-up and wave overtopping at Armored Rubble Slopes and Mounds. In: *Handbook of Coastal and Ocean Engineering*. World Scientific, pp. 605–631.
- Smolka, E., Zarranz, G., Medina, J., 2009. Estudio experimental del rebase de un dique en talud de cubípidos. Libro de Las X Jornadas Españolas de Costas Y Puertos 803–809.
- Stagnitti, M., Iuppa, C., Musumeci, R.E., Foti, E., 2020. Catania harbor breakwater: physical modelling of the upgraded structure. *Coastal Eng. Proc.* 36v.
- Stagnitti, M., Lara, J.L., Musumeci, R.E., Foti, E., 2022. Assessment of the variation of failure probability of upgraded rubble-mound breakwaters due to climate change. *Front. Marine Sci.* 9.
- Stagnitti, M., Lara, J.L., Musumeci, R.E., Foti, E., 2023a. Assessment of the failure probability of upgraded rubble-mound breakwaters. *Coastal Eng. Proc.* 37.
- Stagnitti, M., Musumeci, R., Foti, E., 2023b. Surface roughness measurement for the assessment of damage dynamics of existing and upgraded cube-armored breakwaters. *Coast. Eng.* 179, 104226.
- Steendam, G.J., van der Meer, J.W., Verhaeghe, H., Besley, P., Franco, L., van Gent, M.R., 2005. The international database on wave overtopping. In: *Coastal Engineering 2004*, vol. 4. World Scientific, pp. 4301–4313.
- Takahashi, S., 2002. *Design of Vertical Breakwaters*. PHRI Reference Document Nr. 34.
- Toimil, A., Losada, I.J., Nicholls, R.J., Dalrymple, R.A., Stive, M.J., 2020. Addressing the challenges of climate change risks and adaptation in coastal areas: A review. *Coast. Eng.* 156, 103611.
- van Gent, M., 1999. Physical model investigations on coastal structures with shallow foreshores: 2D model tests with single and double-peaked wave energy spectra. H3608.
- van Gent, M.R., van den Boogaard, H.F., Pozueta, B., Medina, J.R., 2007. Neural network modelling of wave overtopping at coastal structures. *Coast. Eng.* 54, 586–593.
- Victor, L., Van der Meer, J., Troch, P., 2012. Probability distribution of individual wave overtopping volumes for smooth impermeable steep slopes with low crest freeboards. *Coast. Eng.* 64, 87–101.
- Vieira, F., Taveira-Pinto, F., Rosa-Santos, P., 2021. New developments in assessment of wave overtopping on single-layer cube armoured breakwaters based on laboratory experiments. *Coast. Eng.* 166, 103883.
- Williams, H.E., Briganti, R., Pullen, T., 2014. The role of offshore boundary conditions in the uncertainty of numerical prediction of wave overtopping using non-linear shallow water equations. *Coast. Eng.* 89, 30–44.
- Williams, H.E., Briganti, R., Romano, A., Dodd, N., 2019. Experimental analysis of wave overtopping: A new small scale laboratory dataset for the assessment of uncertainty for smooth sloped and vertical coastal structures. *J. Marine Sci. Eng.* 7, 217.
- Zanuttigh, B., van der Meer, J., Bruce, T., Hughes, S., 2014. Statistical characterisation of extreme overtopping wave volumes. In: *From Sea To Shore—Meeting the Challenges of the Sea: (Coasts, Marine Structures and Breakwaters 2013)*. ICE Publishing, pp. 442–451.
- Zanuttigh, B., van der Meer, J.W., 2008. Wave reflection from coastal structures in design conditions. *Coast. Eng.* 55, 771–779.